



Edge-centric functional network representations of human cerebral cortex reveal overlapping system-level architecture

Joshua Faskowitz^{1,2}, Farnaz Zamani Esfahlani¹, Younghun Jo¹, Olaf Sporns^{1,2,3,4} and Richard F. Betzel^{1,2,3,4}  

Network neuroscience has relied on a node-centric network model in which cells, populations and regions are linked to one another via anatomical or functional connections. This model cannot account for interactions of edges with one another. In this study, we developed an edge-centric network model that generates constructs 'edge time series' and 'edge functional connectivity' (eFC). Using network analysis, we show that, at rest, eFC is consistent across datasets and reproducible within the same individual over multiple scan sessions. We demonstrate that clustering eFC yields communities of edges that naturally divide the brain into overlapping clusters, with regions in sensorimotor and attentional networks exhibiting the greatest levels of overlap. We show that eFC is systematically modulated by variation in sensory input. In future work, the edge-centric approach could be useful for identifying novel biomarkers of disease, characterizing individual variation and mapping the architecture of highly resolved neural circuits.

Network science offers a promising framework for representing and modeling neural systems¹. From interconnected cells², to neuronal populations³, to large-scale brain areas⁴, network analysis has contributed insights into the topological principles that govern nervous system organization and shape brain function. These include small-world architecture⁵, the emergence of integrative hubs and rich clubs⁶, modular structure to promote specialized information processing⁷ and tradeoffs between topological features and the material and metabolic costs of wiring⁸.

Central to these and other discoveries in network neuroscience is a simple representation of the brain in which neural elements and their pairwise interactions are treated as the nodes and edges of a network, respectively⁹. This standard model is fundamentally node-centric in that it treats neural elements (nodes) as the irreducible units of brain structure and function. This emphasis on network nodes is further reinforced by the analyses carried out on brain networks, which tend to focus on properties of nodes or groups of nodes—for example, their centralities or community affiliations¹⁰.

A limitation of the node-centric approach is that it cannot capture potentially meaningful features or patterns of inter-relationships among edges. In other scientific domains, prioritizing network edges—for example, by modeling and analyzing edge–edge interactions as a graph—has provided important insights into the organization and function of complex systems^{11,12}. Nonetheless, network neuroscience has remained largely focused on nodal features and partitions, paralleling a rich history of parceling, mapping and comparing cortical and subcortical gray matter regions¹³. On the other hand, several recent studies have begun modeling brain networks from the perspective of interacting edges, including one foundational study that applied graph theoretic measures to a 'line graph'¹² of interrelated white matter tracts¹⁴. Although highly novel, line graphs were never adopted widely, as their construction requires

users to first specify and then apply a sparsity threshold to a connectivity matrix.

Here we present a novel modeling framework for investigating functional brain network data from an edge-centric perspective. Our approach can be viewed as a temporal 'unwrapping' of the Pearson correlation measure—the metric commonly used for estimating the strength of functional connectivity between pairs of brain regions¹⁵—thereby generating interpretable time series for each edge that express fluctuations in its weight across time. Importantly, edge time series allow the estimation of edge correlation structure, a construct we refer to as eFC. High-amplitude eFC indexes strong similarity in the co-fluctuation of two edges across time, whereas low-amplitude eFC indicates co-fluctuation patterns that are largely independent.

From a neuroscientific perspective, eFC can be viewed both as an extension of and a complement to traditional node-centric representations of brain networks. In node-centric network models, functional connections represent the temporal correlation of activity recorded from spatially distinct regions and often interpreted as a measure of inter-regional communication¹⁶. That is, strong functional connections are thought to reflect the time-averaged strength of 'communication' between brain regions. eFC, on the other hand, tracks how communication patterns evolve over time and ultimately assesses whether similar patterns are occurring in the brain simultaneously (Supplementary Fig. 1).

In this study, we demonstrate that eFC is highly replicable given sufficient amounts of data, stable within individuals across multiple scan sessions and consistent across datasets. Next, we apply data-driven clustering algorithms to eFC, which result in partitions of the eFC network into communities of co-fluctuating edges. Each community can be mapped back to individual nodes, yielding overlapping regional community assignments. We find that

¹Department of Psychological and Brain Sciences, Indiana University, Bloomington, IN, USA. ²Program in Neuroscience, Indiana University, Bloomington, IN, USA. ³Cognitive Science Program, Indiana University, Bloomington, IN, USA. ⁴Network Science Institute, Indiana University, Bloomington, IN, USA.

e-mail: rbetzel@indiana.edu

brain regions associated with sensorimotor and attention networks participate in disproportionately many communities compared to other brain systems, but that, relative to one another, those same regions participate in similar sets of communities. Finally, we compare the organization of eFC at rest and during passive viewing of movies and find that eFC is consistently and reliably modulated by changes in sensory input.

Results

In this section, we analyze eFC estimated using functional MRI (fMRI) data from three independently acquired datasets: 100 unrelated participants from the Human Connectome Project (HCP)¹⁷, ten participants scanned ten times as part of the Midnight Scan Club (MSC)¹⁸ and ten participants scanned multiple times as part of the Healthy Brain Network (HBN) Serial Scanning Initiative¹⁹.

eFC. Many studies have investigated networks whose nodes and edges represent brain regions and pairwise functional interactions, respectively⁴. Here we extend this framework to consider interactions not between pairs of brain regions but between pairs of edges.

Extant approaches for estimating edge–edge connectivity matrices include construction of line graphs¹² or calculating edge overlap indices¹¹. Although suitable for sparse networks with positively weighted edges, these approaches are less appropriate for functional neuroimaging data, where networks are typically fully weighted and signed. Here we introduce a method that is well suited for these types of data, operates directly on time series and is closely related to the Pearson correlation coefficient typically used to assess strength of inter-regional functional connections. We refer to the matrices obtained using this procedure as eFC.

Beginning with regional time series, calculating eFC can be accomplished in three steps, starting by z-scoring the time series (Fig. 1a,d). Next, for all pairs of brain regions, we calculate the element-wise product of their z-scored time series (Fig. 1b,e). This results in a new set of time series, referred to as ‘edge time series’, whose elements represent the instantaneous co-fluctuation magnitude between pairs of brain regions and whose average across time is exactly equal to the Pearson correlation coefficient (Fig. 1c)²⁰. Co-fluctuation values are positive when activity of two regions deflects in the same direction at precisely the same moment in time, are negative when activity deflects in the opposite direction and are zero when activity is close to baseline. Importantly, the magnitude of these edge time series is not systematically related to in-scanner motion (Supplementary Fig. 2). The third and final step involves calculating the element-wise product between pairs of edge time series. When repeated over all pairs of edges, the result is an edge-by-edge matrix whose elements are normalized to the interval $[-1,1]$ (Figs. 1f and 2a; see Methods for additional details on eFC construction).

Although eFC is, to our knowledge, a novel construct, we note that the first two steps in calculating eFC are the same as those used to calculate nodal functional connectivity (nFC); the mean value of any co-fluctuation time series is simply the Pearson correlation coefficient. Given that eFC is mathematically related to nFC, we first asked whether it was possible to approximate eFC using estimates of nFC. This is an important question. Whereas the calculation of eFC can be implemented efficiently, performing certain operations on the eFC matrix can prove computationally expensive (it is a fully weighted $[M \times M]$ matrix, where $M = \frac{N(N-1)}{2}$, and N is the number of nodes; Fig. 2b). However, a direct comparison of eFC and nFC is not possible owing to differences in dimensionality. Still, we can approximate eFC using nFC edge weights. Perhaps the simplest approach is to model the edge connection between region pairs $\{i,j\}$ and $\{u,v\}$ as a linear combination of the six edges that can be formed between those regions (Methods). Although this model performs poorly (correlation of observed and approximated eFC; $r=0.21$; $n=197,995,050$ edge–edge pairs), we can improve on its

performance by including interaction terms based on node connectivity—that is, $nFC_{ij} \times nFC_{uv}$ ($r=0.73$; $P < 10^{-15}$; $n=197,995,050$ edge–edge pairs; Fig. 2c). Collectively, these observations suggest that eFC is not well approximated using linear combinations of nFC, but, with nonlinear transformations and inclusion of interaction terms, nFC can approximate eFC. However, these transformations are unintuitive, and the approximation still fails to fully explain variance in eFC.

Next, we explored variation of eFC across acquisitions and processing decisions. We found that eFC weights are similar across three independently acquired datasets (Supplementary Fig. 3) and that the omission of global signal regression from our pre-processing pipeline induced a consistent upward shift of eFC weights, analogous to its effect on nFC (Supplementary Fig. 4). Additionally, we found that the overall pattern of eFC calculated using edge time series estimated from observed data was uncorrelated with the pattern of eFC calculated using edge time series estimated from phase-randomized surrogate time series (Supplementary Fig. 5).

Next, we asked whether eFC exhibits any clear spatial dependence, as nFC is known to decay as a function of Euclidean distance²¹. We assessed the spatial dispersion of eFC with the surface area of the quadrilateral formed by the centroids of the brain region pairs (we explore an alternative edge-level distance metric in Supplementary Fig. 6). We found evidence of a weak negative relationship between surface area and eFC ($r=-0.14$, $P < 10^{-15}$; $n=197,995,050$ edge–edge pairs; Fig. 2d), suggesting that, unlike traditional nFC, whose connection weights are more strongly influenced by spatial relationships of brain areas to one another, eFC is less constrained by the brain’s geometry.

Finally, we asked whether eFC bears the imprint of nFC communities—brain regions whose activity is highly correlated with members of its own community but weakly correlated or anti-correlated with members of other communities⁷. To address this question, we classified every edge in the nFC network according to whether it fell within or between brain systems²², resulting in three possible combinations of connections in the eFC graph: eFC could link edges that both fell within a community, edges that both fell between communities or an edge that fell within and an edge that fell between communities. In general, we found that eFC was significantly stronger for within-community edges compared to the other two categories (Fig. 2e). Interestingly, we found that eFC could be distinguished further by dividing within-community edges by cognitive system²² (one-way analysis of variance (ANOVA); $F_{15,65819}=2,667.4$, $P < 10^{-15}$; Fig. 2f).

eFC is stable within individuals. In this section, we describe the robustness of eFC to scan duration—that is, how much data are required before eFC stabilizes and whether eFC is consistent across repeated scans of the same individual. To address these questions, we leveraged the within-individual design of the MSC dataset. For each participant, we aggregated their fMRI data across all scan sessions and estimated a single eFC matrix. Then, we sampled smaller amounts of temporally contiguous data, thus approximately preserving the auto-correlation structure, and estimated eFC, which we compared against the aggregated eFC matrix (this procedure was repeated 25 times). Similarly to other studies²³, we found that, with small amounts of data, eFC was highly variable (Fig. 3a). However, we observed a monotonic increase in similarity as a function of time, so that, with 30 min of data, the similarity was much greater ($r=0.78$; $P < 10^{-15}$; $n=197,995,050$ edge–edge pairs). This is of practical significance; like traditional nFC, it implies that eFC estimated using data from short scan sessions might not deliver accurate representations of an individual’s edge network organization. We note that this relationship is strengthened when data are sub-sampled randomly and uniformly ($r=0.90$; $P < 10^{-15}$; $n=197,995,050$ edge–edge pairs; Supplementary Fig. 7).

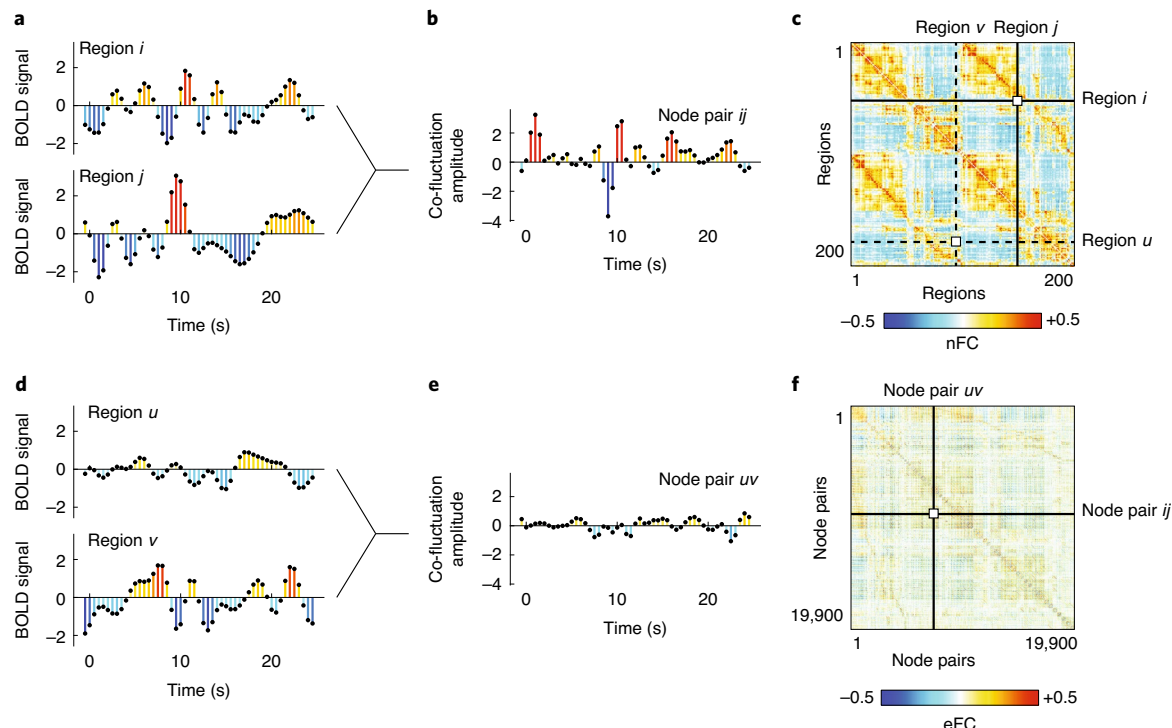


Fig. 1 | Derivation of the eFC matrix. Each element of the eFC matrix is calculated based on the fMRI BOLD activity time series from four nodes (brain regions). **a,d**, We show four representative time series from regions i, j, u and v . **c**, nFC is typically calculated by standardizing (z-scoring) each time series, performing an element-wise product (dot product) of time series pairs and calculating the average value of a product time series (actually the sum of each element divided by $T - 1$, where T is the number of observations). To calculate eFC, we retain the vectors of element-wise products for every pair of regions. **b,e**, We show product time series for the pairs $\{i,j\}$ and $\{u,v\}$, respectively. The elements of these product time series represent the magnitude of time-resolved co-fluctuation between region pairs (or edges in the nFC graph). We can calculate the magnitude of eFC by performing an element-wise multiplication of the product time series and normalizing the sum by the squared root standard deviations of both time series, ensuring that the magnitude of eFC is bounded to the interval $[-1,1]$. **f**, The resulting value is stored in the eFC matrix.

Next, we examined the reliability of eFC over multiple scan sessions. That is, if we imaged an individual on separate days, would their eFC on those days be more similar to each other than to that of a different individual? We estimated eFC and calculated the pairwise similarity (Pearson correlation) between all pairs of MSC participants and scans. We found eFC to be highly reliable in the MSC dataset, where the mean within-participant similarity was $r = 0.53 \pm 0.10$ compared to $r = 0.30 \pm 0.07$ between participants (two-sample t -test; $(4,948) = 62.98$; $P < 10^{-15}$; Fig. 3b,c). Indeed, we found that, for each eFC matrix, the matrix to which it was most similar belonged to the same participant (100% accuracy). Additionally, eFC exhibited slightly greater differential identifiability compared to nFC (0.224 to 0.210)—calculated as the difference between mean within- and between-participant similarity²⁴. In Fig. 3d, we show the results of applying multi-dimensional scaling to the similarity matrix from Fig. 3b. We found similar results in the HBN and HCP datasets (Supplementary Fig. 8).

Collectively, these findings suggest that eFC exhibits a high level of participant specificity and captures idiosyncratic features of an individual, provided that eFC was estimated over a sufficiently long time period. This observation serves as an important validation of eFC and suggests that eFC might be useful in future applications as substrate for biomarker generation and ‘fingerprinting’²⁶.

The overlapping community structure of human cerebral cortex. Although many studies have investigated the brain’s community structure⁷, most have relied on methodology that forces each brain region into one and only one community. However, partitioning brain regions into non-overlapping communities clashes with

evidence suggesting that cognition and behavior require contributions from regions that span multiple node-defined communities and systems²⁷. Accordingly, a definition of communities is needed that more closely matches the brain’s multifunctional nature and the pervasive overlap of its community structure²⁸.

Although deriving overlapping communities of brain regions can be challenging when using nFC, overlap is inherent (indeed, pervasive¹¹) within the eFC construct. Clustering the eFC matrix assigns each edge to a community. Each edge is associated with two brain regions (the nodes it connects). Thus, edge community assignments can be mapped back onto individual brain regions and, because every region is associated with $N - 1$ edges, allow regions to simultaneously maintain a plurality of community assignments.

In this section, we cluster eFC matrices to discover overlapping communities in human cerebral cortex. More specifically, we use a modified k -means algorithm to partition the eFC matrix into non-overlapping communities and map the edge assignments back to individual nodes.

In Fig. 4, we show representative communities obtained with $k = 10$ (Supplementary Figs. 9 and 10 show examples with different numbers of communities). To demonstrate that the communities capture meaningful variance in our data, we show the edge co-fluctuation time series, the eFC matrix and the community co-assignment matrix reordered according to the derived communities (Fig. 4a-c). Here the elements of the co-assignment matrix represent the probability that two edges were assigned to the same community across partitions as we varied the number of communities from $k = 2$ to $k = 20$.

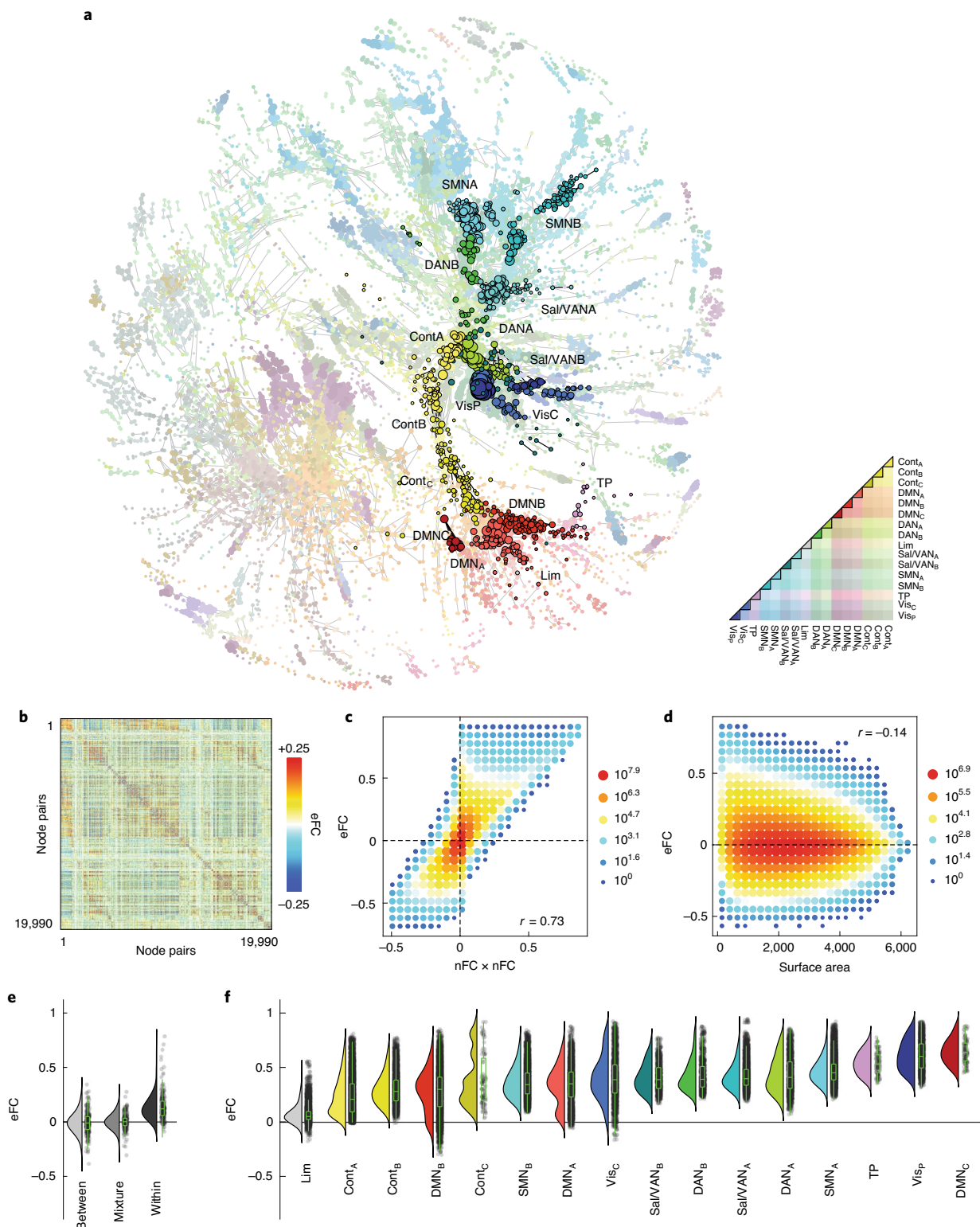


Fig. 2 | Organization of the eFC matrix. **a**, Force-directed layout of the eFC matrix (largest connected component after thresholding away weak connections). Nodes in this graph represent edges in the traditional nFC matrix. Here nodes are colored according to whether the corresponding edge fell within or between cognitive systems. Within-system edges are encircled in black. **b**, eFC matrix in which rows and columns correspond to pairs of brain regions. **c**, Two-dimensional histogram of the relationship between eFC and the product of edges' respective nFC weights. **d**, Two-dimensional histogram of the relationship between eFC and the surface area of the quadrilateral defined by the four nodes. **e**, Mean eFC among edges where both edges fall between systems (between; $n = 2.3 \times 10^8$), where one edge falls within and the other between systems (mixture; $n = 1.7 \times 10^8$) and where both edges fall within systems (within; $n = 8.1 \times 10^5$). **f**, Mean eFC among edges within 16 cognitive systems ($n = 6.5 \times 10^4$). All results presented in this figure are derived from HCP data. Box plots, shown in green and overlaid on data points in **e** and **f**, depict the interquartile range (IQR) and the median value of the distribution. Whiskers extend to the nearest points $\pm 1.5 \times$ IQR above and below the 25th and 75th percentiles. Note that, in **e**, not all points can be displayed owing to the large number of edge-edge connections.

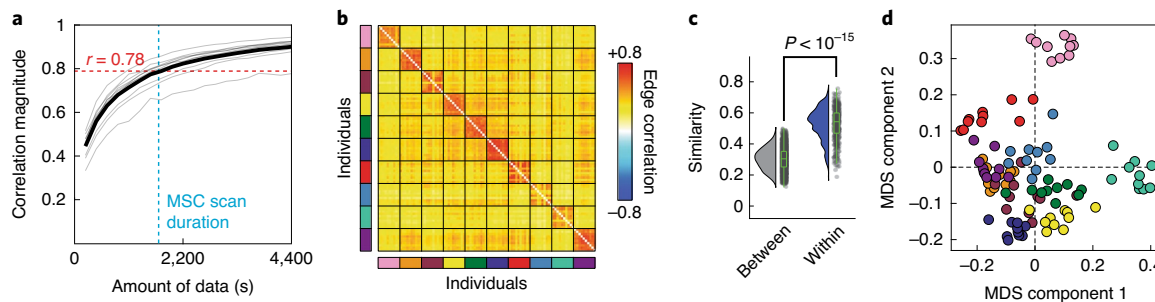


Fig. 3 | Intra- and inter-participant similarity of eFC across scan sessions. **a**, Correlation of session-averaged eFC matrices with eFC estimated using different amounts of data; the mean value is shown as a black line. **b**, Similarity of eFC within and between participants. Each block corresponds to data from a single participant; participants are also identifiable by the color of the rectangle alongside each block. **c**, Violin plots of within- and between-participant similarity values from the matrix shown in **b**; $n_w = 450$ and $n_b = 4,500$ within- and between-participant comparisons (two-sample t -test; $(4,948) = 62.98$; $P < 10^{-15}$). Box plots, shown in green and overlaid on data points in **c**, depict the IQR (box) and the median value of the distribution. Whiskers extend to the nearest points $\pm 1.5 \times$ IQR above and below the 25th and 75th percentiles. **d**, Scan sessions plotted according to coordinates generated by performing a two-dimensional multidimensional scaling (MDS) analysis of the matrix in **b**. Note that scans from the same participant (shown here with the same color) are located near each other. All panels from this figure were generated using data from the MSC.

Although the communities detected here are defined at the level of edges rather than nodes, we can project edge communities back onto brain regions. This was accomplished by extracting the edges associated with each community, determining which nodes were at the endpoints of each edge (the ‘stubs’) and counting the number of times that each node was represented in this stub list. We show these results in matrix form in Fig. 4d. In this panel, rows and columns represent nodes ordered according to the canonical system labels described in ref. ²².

The overlapping nature of communities is made clearer in Fig. 4e, in which communities are represented topographically. The edges associated with the same visual nodes are all involved in communities 7, 8, 9 and 10 to some extent, thereby linking the visual system to multiple other brain systems. In community 8, for example, edges incident upon nodes in the visual and somatomotor systems are clustered together, whereas, in community 9, edges incident upon visual and control network nodes are assigned to the same community.

Community overlap and functional diversity of cognitive systems. In the previous section, we showed that the human cerebral cortex could be partitioned into overlapping communities based on its edge correlation structure. This observation leads to a series of additional questions. For instance, which brain areas participate in many communities? Which participate in few? If we changed the scale of inquiry—the number of detected communities—do the answers to these questions change? Do the answers depend on which dataset we analyze? In this section, we explore these questions in detail.

One strategy for assessing community overlap is to simply count the number of different communities to which each nodes’ edges are assigned²⁹. A more nuanced measure that accounts for the distribution of edge community assignments is the normalized entropy, which indexes the uniformity of a distribution. We therefore calculated normalized entropy for every brain region while varying the number of communities from $k = 2$ to $k = 20$. In this section, we focus on results with $k = 10$.

We found that normalized community entropy was greatest within sensorimotor and attentional systems and lowest within regions traditionally associated with control and default mode networks (Fig. 5a–c). Notably, we obtained similar results from the MSC and HBN datasets (Supplementary Fig. 11), at the level of individual participants (Supplementary Fig. 12), as we varied the number of clusters (Supplementary Fig. 13) and when using different

parcellation schemes (Supplementary Fig. 14). These observations seemingly contradict previous reports in which functional overlap was greatest in control networks and lowest in primary sensory systems (Fig. 5d)^{6,29}.

Is it possible to reconcile these seemingly opposed viewpoints? To address this question, we calculated a second measure of functional diversity. Whereas normalized entropy was defined at the level of individual brain regions based on the edge communities in which they participated, this second measure was defined at the level of brain systems as a whole and assessed the average similarity of edge community assignments among the system regions (Fig. 6a,b and Methods). Intuitively, functionally diverse systems are comprised of brain regions whose edge community assignments are unique and dissimilar from one another. We found that regions within sensorimotor networks, which exhibited among the highest levels of entropy, exhibited the greatest levels of within-system similarity (Fig. 6c). In contrast, sub-networks that make up the control network exhibited the lowest levels of within-system similarity, whereas their constituent nodes had among the lowest entropy (Fig. 6c).

In the Supplementary Material, we explore the relationship of normalized entropy with more familiar measures of overlap derived from nFC, including participation coefficient, dynamic flexibility and versatility (Supplementary Figs. 15 and 16). We also compare patterns of normalized entropy derived from eFC community structure with entropy patterns obtained using alternative methods, including line graphs, the affiliation graph model, Bayesian non-negative matrix factorization and mixed-membership stochastic block models (Supplementary Fig. 17).

eFC is modulated by changes in sensory input. In the previous sections, we demonstrated that eFC is a reliable marker of an individual and that by clustering eFC we naturally obtain overlapping communities. We leveraged this final observation to demonstrate that sensorimotor and attentional systems participate in disproportionately more communities than association cortices. Analogous to previous studies documenting the effect of task on nodal FC, we expect that eFC is also modulated by task.

To address this question, we analyzed fMRI data from the HBN Serial Scanning Initiative recorded during rest and while participants passively viewed the movie ‘Raiders of the Lost Ark’. We estimated group-averaged eFC separately for each of the movie and rest scans.

In general, we found that eFC during movie watching was highly correlated with eFC estimated during rest (Fig. 7a). Across six movie

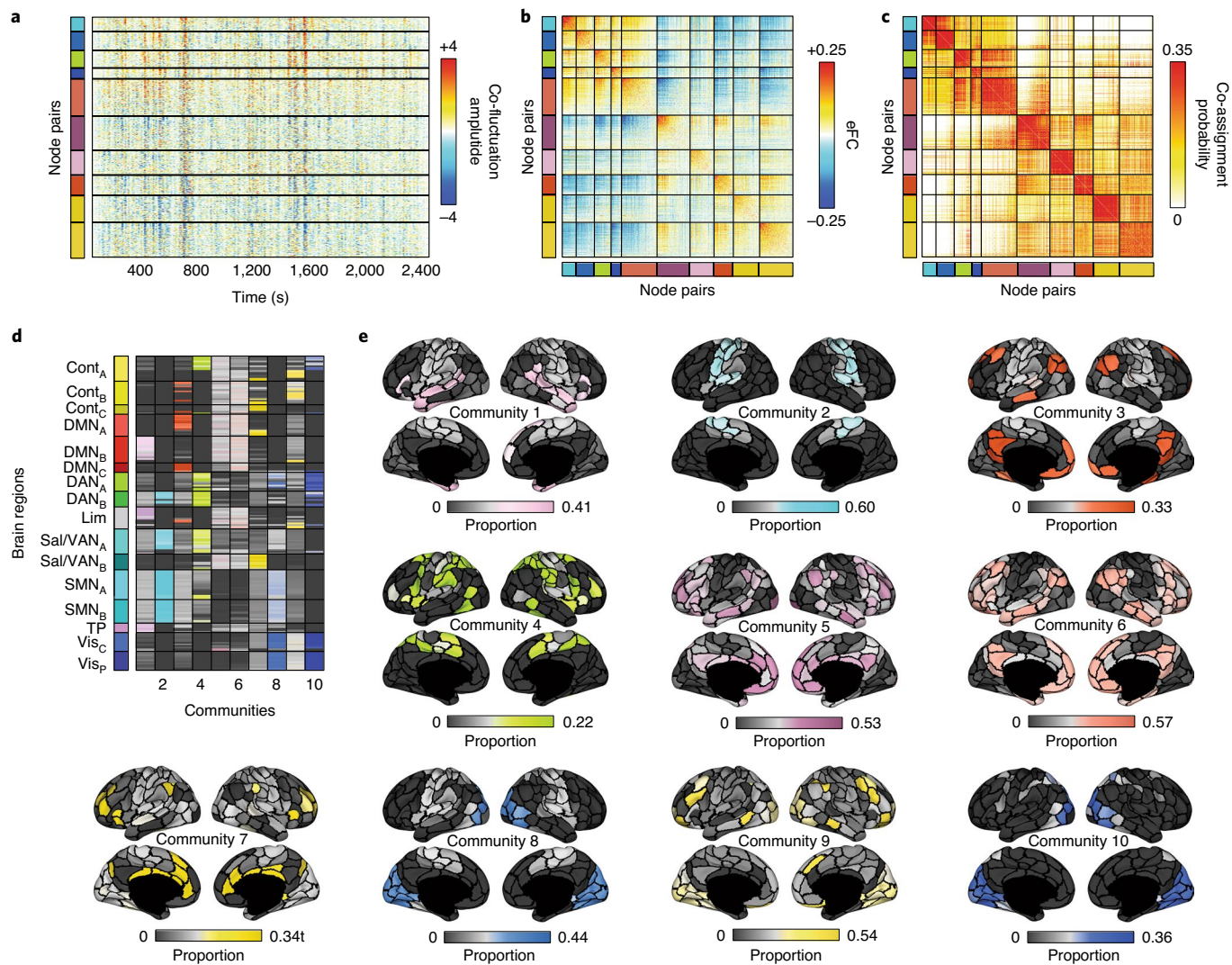


Fig. 4 | Edge communities. We applied similarity-based clustering to eFC from the HCP dataset. Here we show results with the number of clusters fixed at $k = 10$. **a**, Here we reordered edge time series according to the detected community assignments. Horizontal lines divide communities from each other. The colors to the left of the time series plots identify each of the ten communities. **b**, We also reordered the rows and columns of the eFC matrix to highlight the same ten communities. Note that, on average, within-community eFC is greater than between-community eFC. **c**, We calculated the probability that pairs of edges (node pairs) were co-assigned to the same community. Here we show the co-assignment matrix with rows and columns reordered according to community assignments. Note that, in general, the range of co-assignment probabilities goes to 1. Here we truncate the color limits to emphasize the ten-community partition (Supplementary Fig. 9 shows the same co-assignment matrix at different values of k and with non-truncated color limits). We present two visualizations of the edge communities projected back to brain regions (nodes). **d**, We depict overlapping communities in matrix form. Each column in this matrix represents one of ten communities. For each community and for each node, we calculated the proportion of all edges assigned to the community that included that node as one of its endpoints ('stubs'), indicated by the color and brightness of each cell. Dark colors indicate few edges; bright colors indicate many. **e**, Topographic distribution of communities. Note that many of the communities resemble known intrinsic connectivity networks. However, because the communities here can overlap, it is possible for nodes associated with a particular intrinsic connectivity network to participate in multiple edge communities.

scans, the mean correlation with resting eFC was $r = 0.55 \pm 0.02$ (all $P < 10^{-15}$, $n = 197,995,050$ edge–edge pairs). When we compared the pairwise similarity of all movie-watching scans with rest, we found that similarity of eFC was greater within a given task than between tasks ($P < 10^{-4}$, uniform and random permutation of movie and rest conditions; Fig. 7b). To better understand what was driving this effect, we generated representative matrices for rest and movie conditions and computed the element-wise difference between these matrices. We contrasted these differences with those estimated after randomly permuting scan (condition) labels and found that 8.63% of all edge connections exhibited

significant changes between conditions (permutation test; $P < 10^{-4}$; uncorrected). Although eFC differences were widespread, the most pronounced effects were associated with two specific communities (Fig. 7c), one of which exhibited a decrease in its within-module eFC, whereas both decreased eFC with respect to each other. These communities consisted of edges associated with somatomotor and visual systems (Fig. 7d). To confirm that these system-level effects were statistically significant, we compared the mean within- and between-system eFC differences against a constrained null model in which edges communities were randomly permuted (1,000 repetitions; Supplementary Fig. 18 shows a detailed schematic illustrating

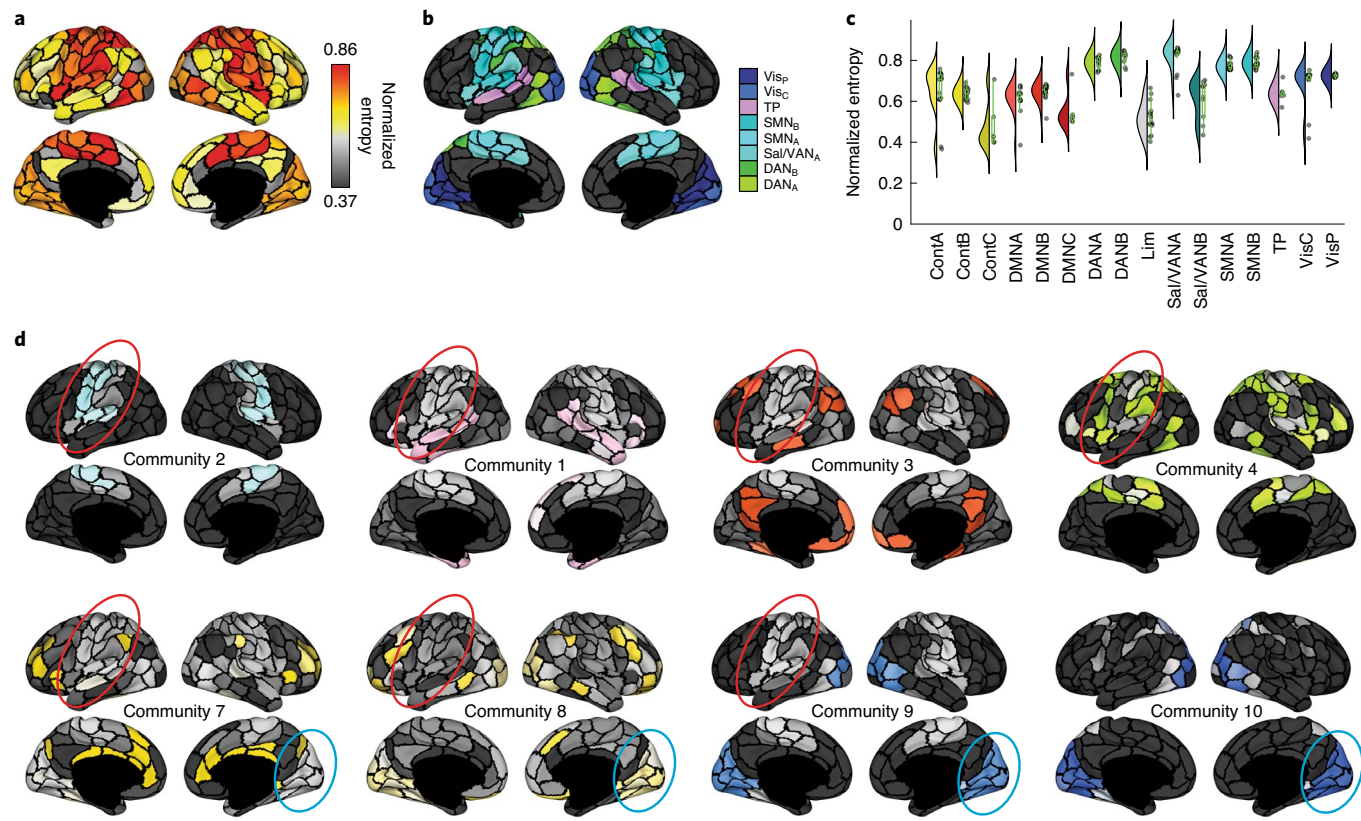


Fig. 5 | Edge community entropy and overlap. **a**, Topographic distribution of normalized entropies. Normalized entropy, in this case, measures the uniformity of a node's community assignments across all communities and serves as a measure of overlap. In general, higher entropy corresponds to greater levels of overlap. **b**, Brain systems associated with the highest levels of normalized entropy. These include visual, attentional, somatomotor and temporoparietal systems. **c**, Entropy values for all brain systems; $n=200$ brain regions. Box plots, shown in green and overlaid on data points, depict the IQR (box) and the median value of the distribution. Whiskers extend to the nearest points $\pm 1.5 \times$ IQR above and below the 25th and 75th percentiles. **d**, Here we highlight communities in which somatomotor (red) and visual (blue) systems are represented.

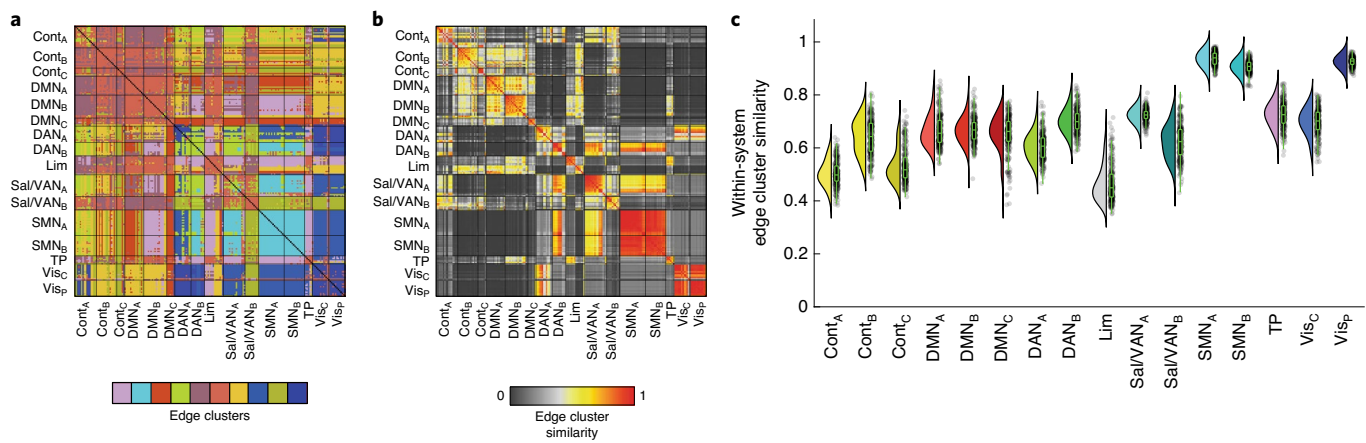


Fig. 6 | System-level similarity of edge communities. **a**, Edge communities can be mapped into a $[N \times N]$ matrix. The element at row i and column j of the edge community matrix denotes the community label of edge $\{i,j\}$. **b**, We can then calculate the similarity of edge communities involving nodes i and j by comparing the values of columns i and j . This matrix depicts the similarity for all pairs of nodes. **c**, Within-system similarity values for each of the 16 pre-defined brain systems; $n=1,272$ within-system similarity values. Box plots, shown in green and overlaid on data points, depict the IQR (box) and the median value of the distribution. Whiskers extend to the nearest points $\pm 1.5 \times$ IQR above and below the 25th and 75th percentiles.

this procedure). As expected, the eFC involving systems 5 and 6 was significantly decreased from rest to movie (permutation test; false discovery rate fixed at 5%; $P_{\text{adjusted}} = 3.7 \times 10^{-5}$). Supplementary Fig. 19a shows the complete list of condition differences.

The differences in the connection weights of eFC between movie watching and rest strongly suggested that the locations of high and low cluster overlap might also differ between conditions. To test this, we used the same clustering algorithm described earlier to partition

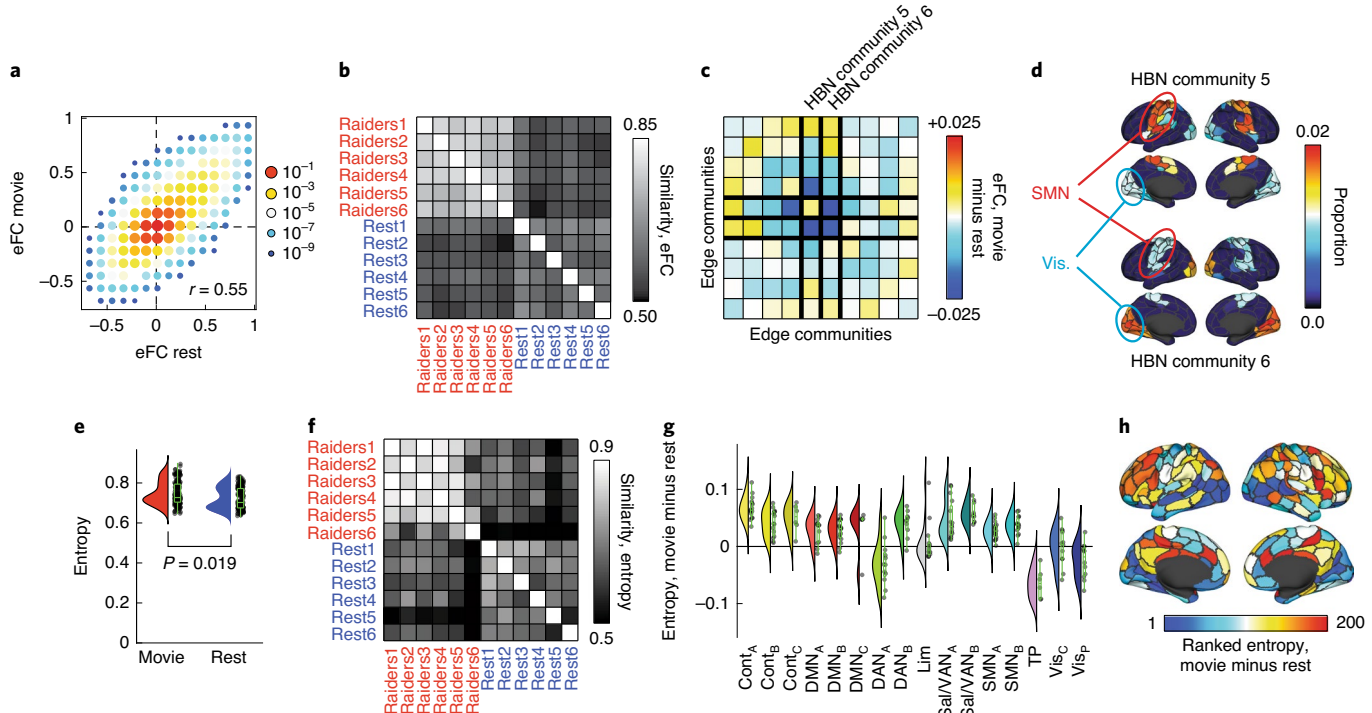


Fig. 7 | Effect of passive movie watching on eFC. **a**, Two-dimensional histogram of eFC estimated at rest with eFC estimated during movie watching. **b**, Similarity of whole-brain eFC estimated at rest with movie watching. Note that within-condition similarity is greater for both conditions. **c**, Community-averaged differences in eFC. Communities 5 and 6 are associated with the largest magnitude differences, on average. Note that these are communities estimated from HBN data and are not identical to those shown in Fig. 4, which were estimated from HCP data. **d**, Topographic distribution of communities 5 and 6. Note that these communities involve edges associated with visual and somatomotor systems. **e**, Averaged differences in community overlap (normalized entropy); $n=200$ brain regions whose entropy scores were compared across rest and movie-watching conditions (permutation test; mean difference in paired samples; $P=0.019$). **f**, Similarity of whole-brain normalized entropy estimated at rest with movie watching. **g**, Violin plot showing system-specific differences in normalized entropy. Note that some of the greatest increases in entropy are concentrated with control and default mode networks; $n=200$ brain regions. **h**, Topographic distribution of differences in entropy. Box plots, shown in green and overlaid on data points in **e** and **g**, depict the IQR (box) and the median value of the distribution. Whiskers extend to the nearest points $\pm 1.5 \times$ IQR above and below the 25th and 75th percentiles.

node pairs into non-overlapping clusters and, based on these clusters, calculated each node's cluster overlap as a normalized entropy. We found that, compared to rest, entropy increased during movie watching (permutation test; mean difference in paired samples; $P=0.019$), indicating increased overlap between communities (Fig. 7e), and that the brain-wide pattern of entropy also differed (permutation test; $P<10^{-4}$; Fig. 7f). We performed analogous tests at the level of individual brain regions and found that 28% of brain regions passed statistical testing (permutation test; false discovery rate fixed at 5%; $P_{adjusted}=0.014$; Supplementary Fig. 19b). We further tested whether these differences exhibited system-specific effects by calculating the mean change in entropy for each system and comparing it against mean changes after randomly and uniformly permuting system labels. We found that seven systems exhibited such effects, with increases concentrated within control and salience/ventral attention networks and decreases in dorsal attention temporal-parietal and visual systems (permutation of system labels; false discovery rate fixed at 5%; $P_{adjusted}=0.012$; Fig. 7g,h and Supplementary Fig. 19c).

Collectively, these results suggest that, like nFC, eFC is reconfigurable and can be modulated by sensory inputs. The observed changes in eFC, which implicated two clusters associated with both somatomotor and visual systems, are in close agreement with past studies of passive movie watching that documented changes in activity and nFC in similar areas³⁰. We also found increased overlap in areas associated with control and default mode networks, which agrees with evidence that activity throughout these areas is sensitive

to movie narrative structure³¹. An important area of future research involves systematically assessing the effect of different cognitively demanding tasks on eFC.

Discussion

Here we presented a network model of human cerebral cortex that focused on edge-edge interactions. The network formed by these interactions—a construct we referred to as eFC—was similar across datasets and more similar within individuals than between them. When clustered, eFC provided a natural estimate of pervasively overlapping community structure. We found that the amount of overlap varied across the cortex but peaked in sensorimotor and attention networks. We found that brain regions associated with sensorimotor and attention networks participated in disproportionately many communities compared to other brain systems, but that, relative to one another, those same regions participated in similar sets of communities. Lastly, we showed that eFC and community overlap varied systematically during passive viewing of movies.

Edge-centric perspective on functional network organization. Node-centric representations have dominated the field of network neuroscience and have served as the basis for nearly every discovery within that field¹. The edge-centric representation shifts focus away from dyadic relationships between nodal activations and, instead, onto the interactions between edges (similarity in patterns of co-fluctuation, a potential hallmark of communication). Although

related models have been explored in other scientific domains^{11,12}, including neuroscience, where they were first used in a study to represent interacting white matter tracts¹⁴, they require, as input, sparse node–node connectivity matrices and are poorly suited for continuous-valued time series data.

In this study, we developed a novel edge-centric representation of functional neuroimaging data that operates directly on observed time series. Our method for estimating connection weights between edges can be viewed as a temporal ‘unwrapping’ of the familiar Pearson correlation—the measure frequently used to estimate the magnitude of nFC between pairs of brain regions. Whereas the Pearson correlation coefficient calculates the time-averaged co-fluctuation magnitude for node pairs, we simply omit the averaging step, yielding ‘edge time series’, which represent the co-fluctuation magnitude between two nodes at every instant in time. This simple step enables us to track fluctuations in edge weight across time and, critically, allow for dyadic relationships between edges, creating an edge-centric representation of nervous system architecture (Fig. 1). If we interpret edge time series as a temporal unwrapping of nFC, which is thought to reflect the aggregate effect of communication processes between neural elements³², then edge times series track, with high temporal resolution, the communication patterns between distributed neural elements.

We note that our edge-centric approach is conceptually similar to several existing methods. For instance, ‘multiplication of temporal derivatives’³³ calculates the element-wise products using differenced activity time series for all pairs of nodes. These time series are then convolved with a kernel to generate smooth estimates of time-varying nFC. Although similar, our approach relies on untransformed activity to estimate edge time series, thereby preserving the relationship between static nFC and the mean value of each edge time series. Another related method is ‘co-activation patterns’ (CAPs)³⁴, which extracts and clusters voxel- or vertex-level activity during high-activity frames. Because a voxel can be co-active under different contexts, the cluster centroids spatially overlap with one another. Although both CAPs and eFC result in overlapping structures, they operate on distinct substrates, with CAPs focusing on activity and eFC focusing on similarity of co-activity. Although CAPs requires the specification of additional parameters compared to eFC—for example, the threshold for a high-activity frame—CAPs might scale better owing to the focus on activity rather than connectivity.

Finally, we note that nFC and eFC are both frameworks for investigating pairwise relationships from neural time series. Critically, however, nFC and eFC differ in terms of what elements are being related to one another and how we interpret those relationships. In the case of nFC, correlations refer to similarities in the activity of individual neural elements, often interpreted as two parts of the brain ‘talking’ to one another. In the case of eFC, on the other hand, correlations express similarities in co-fluctuations along edges, which might loosely be interpreted as ‘conversations’ between node pairs (Supplementary Fig. 1). In other words, nFC focuses on co-activation between nodes whereas eFC focuses on co-fluctuation along edges. In this way, nFC and eFC should be viewed as complementary approaches that can reveal unique organizational features of nervous systems.

Overlapping communities extend understanding of system-level cortical organization. Here we demonstrated that clustering eFC using community detection methods naturally leads to communities that overlap when mapped back to the level of brain regions and nodes. Past investigations of cortical organization have focused almost exclusively on non-overlapping communities. The decision to define communities in this way is partially motivated by interpretability but also by limitations of the methods used to detect communities, which assign nodes to one community only^{35,36}. This

current view of communities has been profoundly successful⁷. It provides a low-dimensional description of the brain, it can be used to define node roles and detect hubs³⁷, and it can be applied to both anatomical and functional networks with equal success.

The dominant non-overlapping perspective of communities has strongly influenced how we think about brain function. Because functional communities exhibit reliable correspondence with patterns of task-evoked activity³⁸, we have come to associate individual communities with specific cognitive domains. For instance, it is not uncommon to refer to communities as primarily processing visual information, enacting cognitive control or performing attentional functions. This localization of brain function to communities, although likely a reasonable first-order approximation, perpetuates a view of brain function in which brain areas, systems and communities are fundamentally unifunctional. Such a view, however, disagrees with observations that many aspects of cognition and behavior transcend these traditional community labels.

Another perspective is that overlap arises from time-varying fluctuations in community structure²⁵. That is, at any given instant, communities are non-overlapping but appear ‘fuzzy’ due to nodes changing their community allegiances over time. The approach developed here is closely aligned with the perspective that brain areas and communities are dynamic and exhibit highly degenerate functionality. Other studies have investigated overlapping and dynamic communities by studying overlap in co-activation or through the use of sliding window analysis and multi-layer models to detect flexible regions that change their community assignment over time. Our approach, however, is distinct, emphasizing a state of pervasive overlap¹¹ in which nodes belong to several communities instantaneously.

Limitations. One of the most important limitations concerns the estimation of edge time series from functional imaging data. To calculate edge time series, we first *z*-scored regional time series. Here, the *z*-score is appropriate only if the time series has a temporally invariant mean and s.d. If there is a sustained increase or decrease in activity—for example, the effect of a blocked task—then the *z*-scoring procedure can result in a biased mean and s.d., resulting in poor estimates of fluctuations in activity. In future work, investigation of task-evoked changes in eFC could be investigated with already common pre-processing steps—for example, constructing task regressors to remove the first-order effect of tasks on activity³⁹.

Another limitation concerns the scalability of eFC. Calculating eFC given for a brain divided into N parcels results in an eFC matrix of dimensions $\frac{N(N-1)}{2}$. This means that an increase in the number of parcels results in a squared increase in the dimensionality of eFC. If the number of parcels is large, this can result in massive, fully weighted matrices that require large amounts of memory to store and manipulate. In the future, however, it might be necessary to explore dimension reduction methods to retain the most relevant sub-graphs for a given task or set of behaviors.

Future directions. Although eFC characterizes interactions between edges rather than nodes, it can still be analyzed using the same methods previously applied to nFC. We can use graph theory to detect its hubs and communities⁶ (Supplementary Fig. 20 shows examples), estimate edge gradients⁴⁰ and compare eFC connection weights across individuals²⁶ and conditions³⁹. On the other hand, eFC affords many new opportunities, beginning with the edge time series used to estimate eFC. Essentially, edge time series offer a moment-to-moment assessment of how strongly two nodes (brain regions) co-fluctuate with one another, providing an estimate of time-varying nFC without the requirement that we specify a window⁴¹. This overcomes one of the main limitations of sliding window estimates of time-varying nFC, namely that the use of a

window leads to a ‘blurring’ of events across time⁴². Other directions for future work include developing whole-brain functional atlases with overlapping system labels and applications to specific brain areas and sub-systems for constructing fine-grained overlapping atlases⁴³. We note, also, that, because the derivation of eFC is based on Pearson correlations, it would be straightforward to estimate analogs of eFC based on lagged and partial relationships.

eFC might be useful in applications of machine learning and classification of neuroimaging data⁴⁴. The dimensionality of the eFC matrix is much greater than that of a typical nFC matrix. We speculate that some of the added dimensions might be useful for studying brain–behavior relationships—for example, by identifying manifolds along which individuals, clinical cohorts or behaviors naturally separate, enhancing classification accuracy⁴⁵ (the results of exploratory analyses of brain–behavior relationships based on eFC are shown in Supplementary Figs. 21–23). On the other hand, the increased dimensionality of eFC requires special considerations, as it presents statistical and interpretational challenges. Multivariate methods⁴⁶, such as canonical correlation analysis or partial least squares, both of which can help circumvent multiple comparison issues, might prove useful and should be investigated in future brain–behavior analysis involving eFC.

Additionally, future studies should investigate appropriate null models for eFC. Like nFC, eFC is correlation based, and the weights of edge–edge connections are not independent of one another⁴⁷. This means that rewiring-based null models (which treat connections as independent) are not appropriate. Consideration should be given to other classes of null models, including time-series-based surrogates. Appropriate null models might help clarify brain–behavior relationships in future studies.

The framework proposed here for investigating interactions between pairs of nodes can be generalized to study mutual interactions between many more nodes by simply calculating the element-wise product of node triplets, quartets and quintets⁴⁸. This extension is, in some respects, analogous to recent applications of algebraic topology⁴⁹, which can uncover higher-order relationships in a network (through graph simplices). We note, however, that, although generating higher-order time series is straightforward, it is necessarily accompanied by an increase in dimensionality, potentially making the approach computationally intractable for whole-brain networks. On the other hand, higher-order time series (and their corresponding eFC analogs) might be useful for investigating the organization of predefined circuits composed of relatively few brain regions or nuclei.

Lastly, the edge-centric framework developed here is not limited to fMRI and can be easily extended to different recording modalities, including scalp/intracranial electroencephalography or magnetoencephalography, which makes it possible to track seizure propagation at the level of edges⁵⁰. Similarly, the application of this approach to datasets resolving single-neuron activity could uncover important connection-level insights into circuit organization³.

Online content

Any methods, additional references, Nature Research reporting summaries, source data, extended data, supplementary information, acknowledgements, peer review information; details of author contributions and competing interests; and statements of data and code availability are available at <https://doi.org/10.1038/s41593-020-00719-y>.

Received: 9 September 2019; Accepted: 3 September 2020;

Published online: 19 October 2020

References

1. Bassett, D. S. & Sporns, O. Network neuroscience. *Nat. Neurosci.* **20**, 353–364 (2017).
2. Schröter, M., Paulsen, O. & Bullmore, E. T. Micro-connectomics: probing the organization of neuronal networks at the cellular scale. *Nat. Rev. Neurosci.* **18**, 131–146 (2017).
3. Dann, B., Michaels, J. A., Schaffelhofer, S. & Scherberger, H. Uniting functional network topology and oscillations in the fronto-parietal single unit network of behaving primates. *eLife* **5**, e15719 (2016).
4. Park, H.-J. & Friston, K. Structural and functional brain networks: from connections to cognition. *Science* **342**, 1238411 (2013).
5. Sporns, O. & Zwi, J. D. The small world of the cerebral cortex. *Neuroinformatics* **2**, 145–162 (2004).
6. Power, J. D., Schlaggar, B. L., Lessov-Schlaggar, C. N. & Petersen, S. E. Evidence for hubs in human functional brain networks. *Neuron* **79**, 798–813 (2013).
7. Sporns, O. & Betzel, R. F. Modular brain networks. *Annu. Rev. Psychol.* **67**, 613–640 (2016).
8. Bullmore, E. & Sporns, O. The economy of brain network organization. *Nat. Rev. Neurosci.* **13**, 336–349 (2012).
9. Bullmore, E. & Sporns, O. Complex brain networks: graph theoretical analysis of structural and functional systems. *Nat. Rev. Neurosci.* **10**, 186–198 (2009).
10. Rubinov, M. & Sporns, O. Complex network measures of brain connectivity: uses and interpretations. *Neuroimage* **52**, 1059–1069 (2010).
11. Ahn, Y.-Y., Bagrow, J. P. & Lehmann, S. Link communities reveal multiscale complexity in networks. *Nature* **466**, 761–764 (2010).
12. Evans, T. & Lambiotte, R. Line graphs, link partitions, and overlapping communities. *Phys. Rev. E* **80**, 016105 (2009).
13. Eickhoff, S. B., Constable, R. T. & Yeo, B. T. Topographic organization of the cerebral cortex and brain cartography. *Neuroimage* **170**, 332–347 (2018).
14. de Reus, M. A., Saenger, V. M., Kahn, R. S. & van den Heuvel, M. P. An edge-centric perspective on the human connectome: link communities in the brain. *Philos. Trans. R. Soc. B Biol. Sci.* **369**, 20130527 (2014).
15. Smith, S. M. et al. Network modelling methods for fMRI. *Neuroimage* **54**, 875–891 (2011).
16. Reid, A. T. et al. Advancing functional connectivity research from association to causation. *Nat. Neurosci.* **22**, 1751–1760 (2019).
17. Van Essen, D. C. et al. The WU-Minn Human Connectome Project: an overview. *Neuroimage* **80**, 62–79 (2013).
18. Gordon, E. M. et al. Precision functional mapping of individual human brains. *Neuron* **95**, 791–807 (2017).
19. O’Connor, D. et al. The healthy brain network serial scanning initiative: a resource for evaluating inter-individual differences and their reliabilities across scan conditions and sessions. *Gigascience* **6**, giw011 (2017).
20. van Oort, E. S. et al. Functional parcellation using time courses of instantaneous connectivity. *Neuroimage* **170**, 31–40 (2018).
21. Esfahlani, F. Z., Bertolero, M. A., Bassett, D. S. & Betzel, R. F. Space-independent community and hub structure of functional brain networks. *Neuroimage* **211**, 116612 (2020).
22. Schaefer, A. et al. Local–global parcellation of the human cerebral cortex from intrinsic functional connectivity MRI. *Cereb. Cortex* **28**, 3095–3114 (2018).
23. Laumann, T. O. et al. Functional system and areal organization of a highly sampled individual human brain. *Neuron* **87**, 657–670 (2015).
24. Amico, E. & Goñi, J. The quest for identifiability in human functional connectomes. *Sci. Rep.* **8**, 8254 (2018).
25. Bassett, D. S. et al. Dynamic reconfiguration of human brain networks during learning. *Proc. Natl. Acad. Sci. USA* **108**, 7641–7646 (2011).
26. Finn, E. S. et al. Functional connectome fingerprinting: identifying individuals using patterns of brain connectivity. *Nat. Neurosci.* **18**, 1664–1671 (2015).
27. Anderson, M. L., Kinnison, J. & Pessoa, L. Describing functional diversity of brain regions and brain networks. *Neuroimage* **73**, 50–58 (2013).
28. Pessoa, L. Understanding brain networks and brain organization. *Phys. Life Rev.* **11**, 400–435 (2014).
29. Yeo, B. T., Krienen, F. M., Chee, M. W. & Buckner, R. L. Estimates of segregation and overlap of functional connectivity networks in the human cerebral cortex. *Neuroimage* **88**, 212–227 (2014).
30. Wilf, M. et al. Spontaneously emerging patterns in human visual cortex reflect responses to naturalistic sensory stimuli. *Cereb. Cortex* **27**, 750–763 (2017).
31. Baldassano, C., Hasson, U. & Norman, K. A. Representation of real-world event schemas during narrative perception. *J. Neurosci.* **38**, 9689–9699 (2018).
32. Avena-Koenigsberger, A., Misic, B. & Sporns, O. Communication dynamics in complex brain networks. *Nat. Rev. Neurosci.* **19**, 17 (2018).
33. Shine, J. M. et al. Estimation of dynamic functional connectivity using multiplication of temporal derivatives. *Neuroimage* **122**, 399–407 (2015).
34. Liu, X. & Duyn, J. H. Time-varying functional network information extracted from brief instances of spontaneous brain activity. *Proc. Natl. Acad. Sci. USA* **110**, 4392–4397 (2013).
35. Newman, M. E. & Girvan, M. Finding and evaluating community structure in networks. *Phys. Rev. E* **69**, 026113 (2004).

36. Rosvall, M. & Bergstrom, C. T. Maps of random walks on complex networks reveal community structure. *Proc. Natl Acad. Sci. USA* **105**, 1118–1123 (2008).
37. Bertolero, M. A., Yeo, B. T. & D’Esposito, M. The modular and integrative functional architecture of the human brain. *Proc. Natl Acad. Sci. USA* **112**, E6798–E6807 (2015).
38. Smith, S. M. et al. Correspondence of the brain’s functional architecture during activation and rest. *Proc. Natl Acad. Sci. USA* **106**, 13040–13045 (2009).
39. Cole, M. W. et al. Task activations produce spurious but systematic inflation of task functional connectivity estimates. *Neuroimage* **189**, 1–18 (2019).
40. Margulies, D. S. et al. Situating the default-mode network along a principal gradient of macroscale cortical organization. *Proc. Natl Acad. Sci. USA* **113**, 12574–12579 (2016).
41. Esfahlani, F. Z. et al. High-amplitude co-fluctuations in cortical activity drive functional connectivity. Preprint at *bioRxiv* <https://doi.org/10.1101/800045> (2020).
42. Lurie, D. J. et al. Questions and controversies in the study of time-varying functional connectivity in resting fMRI. *Netw. Neurosci.* **4**, 30–69 (2020).
43. King, M., Hernandez-Castillo, C. R., Poldrack, R. A., Ivry, R. B. & Diedrichsen, J. Functional boundaries in the human cerebellum revealed by a multi-domain task battery. *Nat. Neurosci.* **22**, 1371–1378 (2019).
44. Pereira, F., Mitchell, T. & Botvinick, M. Machine learning classifiers and fMRI: a tutorial overview. *Neuroimage* **45**, S199–S209 (2009).
45. Huys, Q. J., Maia, T. V. & Frank, M. J. Computational psychiatry as a bridge from neuroscience to clinical applications. *Nat. Neurosci.* **19**, 404 (2016).
46. McIntosh, A. R. & Mišić, B. Multivariate statistical analyses for neuroimaging data. *Annu. Rev. Psychol.* **64**, 499–525 (2013).
47. Zalesky, A., Fornito, A. & Bullmore, E. On the use of correlation as a measure of network connectivity. *Neuroimage* **60**, 2096–2106 (2012).
48. Owen, L. L., Chang, T. H. & Manning, J. R. High-level cognition during story listening is reflected in high-order dynamic correlations in neural activity patterns. Preprint at *bioRxiv* <https://doi.org/10.1101/763821> (2019).
49. Sizemore, A. E., Phillips-Cremins, J. E., Ghrist, R. & Bassett, D. S. The importance of the whole: topological data analysis for the network neuroscientist. *Netw. Neurosci.* **3**, 656–673 (2019).
50. Khambhati, A. N. et al. Dynamic network drivers of seizure generation, propagation and termination in human neocortical epilepsy. *PLoS Comput. Biol.* **11**, e1004608 (2015).

Publisher’s note Springer Nature remains neutral with regard to jurisdictional claims in published maps and institutional affiliations.

© The Author(s), under exclusive licence to Springer Nature America, Inc. 2020

Methods

In this study, we used data from three independently acquired, openly available neuroimaging datasets^{17–19} and, therefore, did not collect any data for this study. No statistical methods were used to pre-determine sample sizes, but our sample sizes are similar to those reported in previous publications^{6,14,18,26,51,52}, and represent either all usable data (MSC and HBN) or a subset pre-selected by the study coordinators (HCP). We did not perform any randomization of participants into experimental groups, and we opted to analyze each dataset separately. Appropriate counterbalancing of task conditions was performed by the authors of the original studies^{17–19}. Data analysis was not performed blinded to the conditions of the experiments. Blinding was not relevant because participants were not evaluated based on group membership, and blinding is not applicable to the whole-group analyses reported in this study. All analyses were performed with MATLAB (MathWorks, Inc.) version 2019a. Further study design and statistical details can be found in the Life Sciences Reporting Summary available online.

Datasets. The HCP dataset¹⁷ included resting state functional magnetic resonance imaging (rsfMRI) data from 100 unrelated adult participants (54% female; mean age = 29.11 ± 3.67 years; age range, 22–36 years). These participants were selected as they comprised the ‘100 Unrelated Subjects’ released by the HCP. The study was approved by the Washington University Institutional Review Board, and informed consent was obtained from all participants. Participants underwent four 15-min rsfMRI scans over a 2-day period. A full description of the imaging parameters and image pre-processing can be found in ref. ⁵³. The rsfMRI data were acquired with a gradient-echo echo-planar imaging (EPI) sequence (run duration = 14:33 min, TR = 720 ms, TE = 33.1 ms, flip angle = 52°, 2-mm isotropic voxel resolution, multi-band factor = 8) with eyes open and instructions to fixate on a cross. Images were collected on a 3T Siemens Connectome Skyra with a 32-channel head coil.

The MSC dataset¹⁸ included rsfMRI from 10 adults (50% female; mean age = 29.1 ± 3.3 years; age range, 24–34 years). The study was approved by the Washington University School of Medicine Human Studies Committee and Institutional Review Board, and informed consent was obtained from all participants. Participants underwent 12 scanning sessions on separate days, each session beginning at 24:00. Ten rsfMRI scans per participant were collected with a gradient-echo EPI sequence (run duration = 30 min, TR = 2,200 ms, TE = 27 ms, flip angle = 90°, 4-mm isotropic voxel resolution) with eyes open and with eye tracking recording to monitor for prolonged eye closure (to assess drowsiness). Images were collected on a 3T Siemens Trio.

The HBN Serial Scanning Initiative dataset¹⁹ included rsfMRI and movie-watching functional magnetic resonance imaging (mvfMRI) from 13 adults (54% female; mean age = 30.3 ± 6.4 years; age range, 21–42 years). Three participants of the HBN dataset did not have enough non-outlier functional scans (see quality control criteria below) to be meaningfully analyzed (non-outlier scan percentage = 7%, 0% and 0%) and were excluded entirely from the current study. This rendered the HBN dataset as ten participants (50% female; mean age = 29.8 ± 5.3 years; age range, 23–37 years). The study was approved by the Chesapeake Institutional Review Board, and informed consent was obtained from all participants. Participants underwent 14 scanning sessions over a 1–2-month period, in which 13 rsfMRI runs were acquired per participant. On the eighth session, participants viewed the movie ‘Raiders of the Lost Ark’ (Lucasfilm) in six approximately 20-min scans. The rsfMRI and mvfMRI were acquired with a gradient-echo EPI sequence (run duration rsfMRI = 10:18 min per segment, run duration mvfMRI = 20 min per segment, TR = 1,450 ms, TE = 40 ms, flip angle = 55°, $2.46 \times 2.46 \times 2.5$ -mm voxel resolution, multi-band factor = 3) with participants instructed to keep their eyes open and gaze directed toward a cross during the fsMRI scan. Images were collected on a 1.5T Siemens Avanto with a 32-channel head coil. The mvfMRI was divided into six successive scan sessions, which we further truncated by retaining the first 420 samples so that the duration matched that of the HBN rsfMRI, of which we retained the first six for the sake of balance.

Image pre-processing. HCP functional pre-processing. Functional images in the HCP dataset were minimally pre-processed according to the description provided in ref. ⁵³. Briefly, these data were corrected for gradient distortion, susceptibility distortion and motion and then aligned to a corresponding T1-weighted (T1w) image with one spline interpolation step. This volume was further corrected for intensity bias and normalized to a mean of 10,000. This volume was then projected to the 32k_fs_LR mesh, excluding outliers, and aligned to a common space using a multi-modal surface registration²⁴. The resultant CIFTI file for each HCP individual who participated in this study followed the file naming pattern *REST{1,2}_{LR,RL}_Atlas_MSKAll.dtseries.nii.

MSC and HBN functional pre-processing. Functional images in the MSC and HBN datasets were pre-processed using fMRIprep 1.3.2 (ref. ⁵⁵), which is based on Nipype 1.1.9 (ref. ⁵⁶). The following description of fMRIprep’s pre-processing is based on boilerplate distributed with the software covered by a ‘no rights reserved’ (CC0) license. Internal operations of fMRIprep use Nilearn 0.5.0 (ref. ⁵⁷), ANTs 2.2.0, FreeSurfer 6.0.1, FSL 5.0.9 and AFNI v16.2.07. For more details about the pipeline, see the section corresponding to workflows in fMRIprep’s documentation.

T1w images were corrected for intensity non-uniformity with N4BiasFieldCorrection^{58,59}, distributed with ANTs and used as T1w-reference throughout the workflow. The T1w-reference was then skull-stripped with a Nipype implementation of the antsBrainExtraction.sh workflow, using NKI as the target template. Brain surfaces were reconstructed using recon-all⁶⁰, and the brain mask estimated previously was refined with a custom variation of the method to reconcile ANTs-derived and FreeSurfer-derived segmentations of the cortical gray matter using Mindboggle⁶¹. Spatial normalization to the ICBM 152 Nonlinear Asymmetrical template version 2009⁶² was performed through nonlinear registration with antsRegistration, using brain-extracted versions of both T1w volume and template. Brain tissue segmentation of cerebrospinal fluid, white matter and gray matter was performed on the brain-extracted T1w images using FSL’s fast⁶³.

Functional data were slice-time corrected using AFNI’s 3dTshift and motion corrected using FSL’s mcflirt⁶⁴. Fieldmap-less distortion correction was performed by co-registering the functional image to the same-participant T1w image with intensity inverted⁶⁵ and constrained with an average fieldmap template⁶⁶, implemented with antsRegistration. This was followed by co-registration to the corresponding T1w image using boundary-based registration⁶⁷ with 9° of freedom. Motion-correcting transformations, field-distortion-correcting warp, BOLD-to-T1w transformation and T1w-to-template (MNI) warp were concatenated and applied in a single step using antsApplyTransforms using Lanczos interpolation. Several confounding time series were calculated based on this pre-processed BOLD: framewise displacement (FD), DVARS and three region-wise global signals. FD and DVARS are calculated for each functional run, both using their implementations in Nipype⁶⁸. The three global signals are extracted within the cerebrospinal fluid, the white matter and the whole-brain masks. The resultant nifti file for each MSC and HBN individual who participated in this study followed the file naming pattern *space-T1w_desc-preproc_bold.nii.gz.

Image quality control. All functional images in the HCP and MSC datasets were retained. The quality of functional images in the MSC and HBN datasets were assessed using fMRIprep’s visual reports and MRIQC 0.15.1 (ref. ⁶⁹). Data were visually inspected for whole-brain field of view coverage, signal artifacts and proper alignment to the corresponding anatomical image. Functional data were excluded if more than 25% of the frames exceeded 0.2-mm FD⁷⁰. Furthermore, HBN functional data were excluded if marked as an outlier (exceeding 1.5× interquartile range (IQR) in the adverse direction) in more than half of the following image quality metrics (calculated within datasets, across all functional acquisitions): dvars, tsnr, fd mean, aor, aqi, snr and etc. Information about these image quality metrics can be found in MRIQC’s documentation.

Functional and structural networks pre-processing. Parcellation preprocessing. A functional parcellation designed to optimize both local gradient and global similarity measures of the fMRI signal²² (Schaefer200) was used to define 200 areas on the cerebral cortex. These nodes are also mapped to the Yeo canonical functional networks⁷¹. For the HCP dataset, the Schaefer200 is openly available in ‘32k fs LR’ space as a CIFTI file. For the MSC and HBN datasets, a Schaefer200 parcellation was obtained for each participant using a Gaussian classifier surface atlas⁷² (trained on 100 unrelated HCP participants) and FreeSurfer’s mris_ca_label function. These tools use the surface registrations computed in the recon-all pipeline to transfer a group average atlas to subject space based on individual surface curvature and sulcal patterns. This method rendered a T1w space volume for each participant. For use with functional data, the parcellation was resampled to 2-mm T1w space. This process could be repeated for other resolutions of the parcellation (that is, Schaefer100).

Functional network pre-processing. Each pre-processed BOLD image was linearly de-trended, band-pass filtered (0.008–0.08 Hz)⁷⁰, confound regressed and standardized using Nilearn signal.clean, which removes confounds orthogonally to the temporal filters⁷³. The confound regression employed⁷⁴ included six motion estimates; time series of the mean cerebrospinal fluid, mean white matter and mean global signal; the derivatives of these nine regressors; and the squares of these 18 terms. Furthermore, a spike regressor was added for each fMRI frame exceeding a motion threshold (HCP = 0.25-mm root mean squared displacement; MSC and HBN = 0.5-mm FD). This confound strategy has been shown to be a relatively effective option for reducing motion-related artifacts⁷⁰. After pre-processing and nuisance regression, residual mean BOLD time series at each node were recovered. eFC matrices for each participant were computed and then averaged across participants to obtain a representative eFC matrix for each dataset. This processing was performed for both resting-state and movie-watching data.

Edge graph construction. Constructing networks from fMRI data (or any neural time series data) requires estimating the statistical dependency between every pair of time series. The magnitude of that dependency is usually interpreted as a measure of how strongly (or weakly) those voxels or parcels are functionally connected to each other. By far the most common measure of statistic dependence is the Pearson correlation coefficient. Let $x_i = [x_i(1), \dots, x_i(T)]$ and $x_j = [x_j(1), \dots, x_j(T)]$

be the time series recorded from voxels or parcels i and j , respectively. We can calculate the correlation of i and j by first z scoring each time series, such that at $z_i = \frac{x_i - \mu_i}{\sigma_i}$ where $\mu_i = \frac{1}{T} \sum_t x_i(t)$ and $\sigma_i = \sqrt{\frac{1}{T-1} \sum_t (x_i(t) - \mu_i)^2}$ are the time-averaged mean and s.d. Then, the correlation of i and j can be calculated as $r_{ij} = \frac{1}{T-1} \sum_t [z_i(t) \cdot z_j(t)]$. Repeating this procedure for all pairs of parcels results in a node-by-node correlation matrix—that is, an estimate of functional connectivity. If there are N nodes, this matrix has dimensions $[N \times N]$.

To estimate edge-centric networks, we need to modify the above approach in one small but crucial way. Suppose we have two z -scored parcel time series, z_i and z_j . To estimate their correlation, we calculate the mean of their element-wise product (not exactly the average, because we divide by $T-1$ rather than T). Suppose, instead, that we never calculate the mean and simply stop after calculating the element-wise product. This operation would result in a vector of length T whose elements encode the moment-by-moment co-fluctuations magnitude of parcels i and j . For instance, suppose at time t , parcels i and j simultaneously increased their activity relative to baseline. These increases are encoded in z_i and z_j as positive entries in the t th position, so their product is also positive. The same would be true if i and j decreased their activity simultaneously (because the product of negatives is a positive). On the other hand, if i increased while j decreased (or vice versa), this would manifest as a negative entry. Similarly, if either i or j increased or decreased while the activity of the other was close to baseline, the corresponding entry would be close to zero.

Accordingly, the vector resulting from the element-wise product of z_i and z_j can be viewed as encoding the magnitude of moment-to-moment co-fluctuations between i and j . An analogous vector can easily be calculated for every pair of parcels (network nodes), resulting in a set of co-fluctuation (edge) time series. With N parcels, this results in $\frac{N(N-1)}{2}$ pairs, each of length T . From these time series, we can estimate the statistical dependency for every pair of edges. We refer to this construct as eFC. Let $c_{ij} = [z_i(1) \cdot z_j(1), \dots, z_i(T) \cdot z_j(T)]$ and $c_{uv} = [z_u(1) \cdot z_v(1), \dots, z_u(T) \cdot z_v(T)]$ be the time series for edges $\{i,j\}$ and $\{u,v\}$, respectively. Then, we can calculate eFC as

$$eFC_{ij,uv} = \frac{\sum_t c_{ij}(t) \cdot c_{uv}(t)}{\sqrt{\sum_t c_{ij}(t)^2} \sqrt{\sum_t c_{uv}(t)^2}}$$

Here, the denominator is necessary to bind eFC to the interval $[-1,1]$.

Clustering algorithm. In general, eFC matrices are much larger than traditional nFC matrices. Although most clustering algorithms can be applied to hundreds or even thousands of observations, estimating clusters for eFC (which consists of tens of thousands of observations, each paired with at least as many features) presents a computational challenge, especially if the aim is to explore the space of possible partitions. To address this issue and to cluster eFC, we developed a simple two-step clustering procedure that operates on a low-dimensional representation of the eFC matrix.

First, we performed an eigen decomposition of the eFC matrix, retaining the top 50 eigenvectors. Eigenvector coefficients were rescaled to the interval $[-1,1]$ by dividing each by its largest magnitude element, and then the rescaled coefficients were simply clustered using a standard k -means algorithm with Euclidean distance. We varied the number of communities, k , from $k=2$ to $k=20$, repeating the clustering algorithm 250 times at each value. We retained, as a representative partition, the one with the greatest overall similarity to all other partitions. We note that the edge time series can be clustered directly and that, in general, the results were highly similar (Supplementary Fig. 12).

We note that, in general, other community detection algorithms could be used in place of k -means. Our decision to use this algorithm was practically motivated, as k -means exhibited significantly faster runtimes than other algorithms—for example, modularity maximization³⁵ and Infomap³⁶, which have been used extensively in previous work to derive communities in both functional and structural brain networks.

Community overlap metrics. The clustering algorithm partitioned edges into non-overlapping clusters. That is, every edge $\{i,j\}$, where $i,j \in \{1, \dots, N\}$, was assigned to one of the k clusters. In this list of edges, each node appeared $N-1$ times (we excluded self-connections). Region i 's participation in cluster c was calculated as

$$p_{ic} = \frac{1}{N-1} \sum_{j \neq i} \delta(g_{ij}, c)$$

where $g_{ij} \in \{1, \dots, k\}$ was the cluster assignment of the edge linking nodes i and j , and $\delta(x,y)$ is the Kronecker delta, whose value is 1 if $x=y$ and 0 otherwise. By definition, $\sum_c p_{ic} = 1$, and we can treat the vector $p_i = [p_{i1}, \dots, p_{ik}]$ as a probability distribution. The entropy of this distribution measures the extent to which region i 's community affiliations are distributed evenly across all communities (high entropy and high overlap) or concentrated within a small number of communities (low entropy and low overlap). We calculate this entropy as:

$$h_i = - \sum_c p_{ic} \log_2 p_{ic}$$

To normalize this measure and bind it to the interval $[0,1]$, we divided by $\log_2 k$. We refer to this measure as community entropy and interpret this value as an index of overlap. Intuitively, as the distribution of edge community assignments approaches uniformity, its normalized entropy is close to 1; when edges are assigned to a single community, normalized entropy is closer to 0.

Edge community similarity. When we cluster an eFC matrix, we assign each edge to a single community. These edge communities can be rearranged into the upper triangle of an $N \times N$ matrix, X , whose element x_{ij} denotes the edge community assignment of the edge between nodes i and j . The i th column of X , which we denote as $x_i = [x_{i1}, \dots, x_{iN}]$, encodes the community labels of all edges in which node i participates. Note that we do not consider self-edges, so the element x_{ii} is left empty.

From this matrix, we can compare the edge communities of nodes i and j by calculating the similarity of vectors x_i and x_j . Here, we measure that similarity as the fraction of elements in both vectors with the same community label. That is:

$$s_{ij} = \frac{1}{N-2} \sum_{u \neq i,j} \delta(x_{iu}, x_{ju})$$

Here, $\delta(x,y)$ is the Kronecker delta and takes on a value of 1 when x and y have the same value but is 0 otherwise. Note the normalization of over $N-2$ because we ignore the self-connections x_{ii} and x_{jj} . Repeating this comparison for all pairs of nodes generates the similarity matrix $S = \{s_{ij}\}$.

Estimating overlapping community structure from nFC. In this study, we applied a clustering algorithm to eFC, which generates overlapping nodal communities. In contrast, field standard community detection algorithms like Infomap³⁶ and modularity maximization³⁵ partition nFC into non-overlapping communities. However, there are non-standard methods that can be applied directly to nFC that generate overlapping communities. These include, but are not limited to, stochastic variational inference for the mixed-membership stochastic block model⁷⁵ (SVINET), the Affiliation Graph Model⁷⁶ (AGMFIT), Bayesian non-negative matrix factorization⁷⁷ (NMF) and thresholded weighted link clustering^{12,14} (ThrLink).

We applied these methods to group representative nFC data from the HCP dataset (with the number of communities fixed at $k=10$) and compared their patterns of overlap with those obtained from clustering eFC. In general, each of these alternative methods require that the input connectivity matrix contain only positively weighted or binary edges, necessitating that it be thresholded. To do this, we computed the maximum spanning tree of the nFC matrix (to ensure that all nodes form a single connected component) and added edges to this backbone to reach a desired network density. We repeated the following comparisons across densities of 10%, 20%, 30% and 40% (a range in which negative edges were not retained). For each method, 250 overlapping community structures were recovered. We describe each method in more detail below and summarize the results in Supplementary Fig. 17.

The SVINET method employs a mixed-membership stochastic block model algorithm, which is a generative model of network communities based on grouping nodes with similar connectivity patterns⁷⁵. This method has been previously used to demonstrate that the areas of the brain that participate in many cognitive functions also participate in proportionally more communities⁷⁸. This method operates on binary connections; thus, edge weights were discarded. Each run was seeded with a random integer and run for 250 iterations with link sampling. Resulting community assignments with at least 5% membership likelihood were recorded as a membership affiliation.

The AGMFIT method employs a generative model of communities based on a bipartite graph structure, linking nodes to communities⁷⁶. The central concept of the AGMFIT algorithm is that communities overlap in a ‘tiled’ manner, meaning that nodes with overlapping community membership are more densely interconnected than non-overlapping nodes. This model of overlapping structure has been shown to accurately capture core-periphery structure in large-scale social networks. This method operates on binary connections; thus, edge weights were discarded. Each run was seeded with a random integer.

The NMF method employs a probabilistic data reduction model that results in a soft partitioning of the network⁷⁷. This method has been shown to avoid over-fitting communities in synthetic random graph data where no real communities exist. Edge weights were retained for this method, and diagonal entries of the adjacency matrix were set to the nodal degree (as suggested in the documentation). Each run was randomly initialized. Runs that did not produce the desired number of communities were rejected, and sampling continued until 250 partitions were obtained. Resulting community assignments with at least 5% membership likelihood were recorded as membership affiliation.

For the ThrLink method, we created a weighted line graph from the thresholded adjacency matrix¹². This matrix was clustered using the generalized Louvain algorithm with the resolution parameter γ tuned to produce the desired number of communities. To tune this parameter, a range of values was used to recover communities of varying sizes. The minimum and maximum values producing the desired number of communities were recorded. Uniformly

randomly sampled γ values within this range were used to recover communities of the weighted line graph. Runs that did not produce the desired number of communities were rejected, and sampling continued until 250 partitions were obtained. Community memberships of the weighted line graph were projected to the nodes to gather the overlapping structure.

We compared community entropy against a series of related statistics that can be easily derived from nFC as opposed to eFC. These include static measures of participation coefficient⁷⁹ and versatility⁸⁰ and the 'dynamic' measure of flexibility^{25,81}. We calculated static measures using a group representative nFC matrix that was the average nFC data from all scans and individuals. Flexibility was calculated first at the single-individual level where time series were divided into ten non-overlapping windows containing $L = 120$ samples each (approximately 86 s) and subsequently averaged across individuals. Details of how each measure was calculated are presented below.

Participation coefficient measures the uniformity with which a node's connections are distributed across (non-overlapping) communities. Values closer to 1 indicate that connections are distributed evenly. Participation coefficient is calculated as:

$$pc_i = 1 - \sum \left(\frac{k_{is}}{k_i} \right)^2$$

Here, k_i is the total strength of node i , and k_{is} is the strength of node i to community s . We calculated several variants of participation coefficient in which we varied how communities were defined. First, we treated the system labels from ref. ²² as a community structure and calculated the participation coefficient with respect to these labels. We also tested a more data-driven procedure in which we used multi-scale modularity maximization⁸² to detect the communities of the nFC matrix. In doing so, we used a uniform null model^{13,84}, which is appropriate for correlation matrices and has been used extensively in the neuroimaging community (see ref. ⁸⁵ as just one example) and systematically varied the resolution parameter γ over the interval [0,0.5] (repeating a Louvain-like algorithm 1,000 times). In all cases, we separately calculated the participation coefficient using for positive and negative connection weights.

We also used the detected communities to estimate regional versatility⁸⁰, which measures the variability of a node's community assignment across repeated runs of a community detection algorithm. We calculated versatility as:

$$v_i = \frac{\sum_j \sin(\pi \cdot p_{ij})}{\sum_j p_{ij}}$$

For a given value of γ , p_{ij} denotes the fraction of times that nodes i and j were co-assigned to the same community. We calculated versatility with respect to communities detected using the same values of γ .

Lastly, we calculated network flexibility, which measures how frequently a brain region changes communities across time. We modeled functional connectivity estimated within each non-overlapping window as a layer in a multi-layer network and a used multi-layer modularity maximization algorithm⁸⁶ to cluster all layers simultaneously. The result is a node-by-layer matrix of communities whose element g_{is} indicates the community assignment of node i in layer s . From this matrix, we calculate flexibility as:

$$f_i = 1 - \frac{1}{T-1} \sum_{s=1}^{T-1} \delta(g_{is}, g_{i,s+1})$$

Here, $T=10$ is the number of layers, and $\delta(g_{is}, g_{i,s+1})$ is the Kronecker delta function and is equal to 1 when $g_{is} = g_{i,s+1}$ and is 0 otherwise. In essence, flexibility measures the fraction of times that a node's community assignment changes in successive layers (time points). In addition to the γ resolution parameter, the output of the multi-layer modularity maximization algorithm depends on a second parameter, ω , that controls the consistency of communities across layers. We systematically varied these parameters over the ranges $\gamma = [0,0.25,0.5]$ and $\omega = [0.1,0.5,1]$ and calculated flexibility for all possible $\{\gamma, \omega\}$ pairs.

Graph theoretic analysis of eFC. We applied graph theoretic measures to the eFC matrix to characterize its topological features¹⁰. We focused on local measures that characterize features at the level of a network's nodes (in the case of eFC, nodes represent pairs of brain regions). To visualize these measures, we reshaped their values into the upper triangle of a region-by-region matrix (Supplementary Fig. 20). We focused on several different measures:

1. Degree (\pm) measures separately the total number of positive and negative connections incident upon a given node in the eFC network.
2. Strength (\pm) is the weighted analog of degree and measures separately the total weight of positive and negative connections incident upon a given node in the eFC network. Both degree and strength tell us, on average, how strongly or weakly a given node in the eFC network interacts with other nodes in the eFC network.
3. Participation coefficient (\pm) measures the extent to which a node's connections in the eFC network are concentrated within or distributed across edge

communities. Values close to 0 mean that a given node in the eFC network interacts primarily with other nodes in its own edge community; values close to 1 mean that a given node in the eFC network interacts uniformly with all edge communities.

4. Betweenness centrality measures the number of shortest paths between pairs of nodes in the eFC network that pass through a given node. In general, betweenness centrality implies that a particular node in the eFC network might occupy a position of importance in the network.
5. Clustering coefficient measures the extent to which a node's neighbors in the eFC network are also connected to one another.

Exploratory analyses of brain-behavior relationships using eFC. Correlations of eFC weights with behavior. We also used eFC data to explore brain-behavior relationships⁸⁷. The overall pipeline begins by calculating each participant's edge-by-edge eFC matrix (Supplementary Fig. 21a) and representing its upper triangle elements as a vector (Supplementary Fig. 21b). This procedure is repeated for all individuals in the HCP 100 Unrelated Subjects cohort so that the vectorized eFC is stored in a single matrix (Supplementary Fig. 21c). In parallel, we z-scored participants' behavioral data and performed principal components analysis, resulting in a set of scores that characterize orthogonal modes of behavioral variability (Supplementary Fig. 21d and Supplementary Table 1). We computed the correlation of scores with rows from the matrix of vectorized eFC matrices (each row represents the eFC for a particular edge-edge interaction (Supplementary Fig. 21e)). Repeating this procedure for all rows results in a vector of correlation coefficients that can be reshaped to fit into the upper triangle of an edge-by-edge matrix, resulting in a correlation map (Supplementary Fig. 21f). This entire process is repeated separately for principal components 1–10 and for scans REST1 and REST2.

We compared the correlation maps from REST1 and REST2 and found good correspondence (Supplementary Fig. 21h,i). To better interpret these maps, we adopted a community-level analysis (see Supplementary Fig. 22 for a short schematic). Briefly, this involves aggregating and averaging correlation coefficients by edge communities (Supplementary Fig. 22b); comparing the average correlation coefficients against a null distribution obtained using a constrained permutation test (Supplementary Fig. 22c); and performing statistical evaluation, controlling for false discovery rate at the level of communities (Supplementary Fig. 22d). Further details of the permutation test can be found in Supplementary Fig. 18.

Using this community-level approach, we investigated the relationship between eFC and PC1 in greater detail. We note that PC1 explains approximately 17% variance in behavioral data (almost three times as much as PC2) and defines a task accuracy/reaction time axis of behavior (Supplementary Fig. 21j,k). We include brief descriptions of the other PCs in Supplementary Table 1. We show the correlation map for PC1 with eFC in Supplementary Fig. 21l. To illustrate how the community-level analysis facilitates a clearer interpretation of brain-behavior correlations, consider eFC of edges in communities 7 and 9 (the block highlighted in Supplementary Fig. 21l). Community 7 links higher-order cognitive areas in the control and default mode networks with visual cortex, forming an 'executive-visual' complex, whereas community 9 links control and default mode to the salience/ventral attention network as part of an 'executive-insular' complex (Supplementary Fig. 21m,n). Accordingly, the positive correlation eFC between community 7 and 9 with PC1 means that, as the edges within those communities become more synchronized across time (stronger eFC), the value of PC1 increases proportionally (Supplementary Fig. 21o,p).

In addition to modeling brain-behavior relationships using the original eFC data, we repeated this same analysis with residual eFC after regressing out the effect of nFC. Specifically, we used the procedure described in Fig. 2c to generate an approximation of eFC using only nFC data. We then regressed out the approximated eFC from the actual eFC and assessed brain-behavior relationships using the residual values. As with the previous analysis, we found that brain-behavior correlation maps were reproducible across scan sessions (Supplementary Fig. 23).

Correlations of regional statistics with behavior. We also compared eFC and nFC brain-behavior relationships by deriving a series of regional (local) network statistics from each and calculating the correlations of behavioral measures with these statistics (Supplementary Fig. 24). We note that the measures derived from both nFC and eFC have identical dimensionality, effectively accounting for any differences in the dimensionality of the original nFC and eFC matrices. In general, we found that the correlation patterns estimated using nFC-derived statistics were highly similar to one another, whereas the correlation pattern derived from the eFC statistic was dissimilar (Supplementary Fig. 24f).

These findings demonstrate that eFC has the potential to uniquely explain patterns of inter-individual variability not currently explainable by nFC, opening new opportunities for studying individual differences in individuals' cognitive, developmental and clinical states.

Modeling eFC in terms of nFC. eFC and nFC are both derived from the same substrate: regional fMRI BOLD time series. Can the eFC between edges $\{i,j\}$ and $\{u,v\}$ be easily modeled in terms of nFC? We tested whether this was the case using

linear regression to explain the eFC between pairs of edges $\{i,j\}$ and $\{u,v\}$ using information about the pairwise nFC among the same set of nodes: $\{i,j\}$, $\{i,u\}$, $\{i,v\}$, $\{j,u\}$, $\{j,v\}$ and $\{u,v\}$. We considered two classes of models. The first modeled eFC in terms of the six nFC weights:

$$eFC_{ij,uv} = \beta_1 nFC_{ij} + \beta_2 nFC_{iu} + \beta_3 nFC_{iv} + \beta_4 nFC_{ju} + \beta_5 nFC_{jv} + \beta_6 nFC_{uv} + \beta_0 + \epsilon$$

The second modeled eFC in terms of nFC interactions:

$$eFC_{ij,uv} = \beta_1 [nFC_{ij} \times nFC_{uv}] + \beta_0 + \epsilon$$

In this model, we systematically varied the interaction term, $nFC_{ij} \times nFC_{uv}$, so that we tested all possible pairs of edges.

In general, we found that neither model 1 nor model 2 could fully reproduce eFC. Model 1 performed particularly poorly ($r=0.21$). The results of model 2 were more varied. When all nodes were represented in the interaction term—for example, $nFC_{ij} \times nFC_{uv}$ —the model performed well ($r=0.72 \pm 0.05$), consistent with what we reported in Fig. 2c. When any node is repeated—for example, $nFC_{ij} \times nFC_{i^*v}$ —the model performed poorly ($r=0.06 \pm 0.04$).

Collectively, these observations suggest that eFC is not well approximated using linear combinations of nFC, but, with nonlinear transformations and inclusion of interaction terms, nFC can approximate eFC. However, these transformations are unintuitive, and the approximation still fails to fully explain variance in eFC.

Statistics. All statistical comparisons made between individuals and groups were implemented using paired sample and two-sample *t*-tests, ANOVAs or permutation tests. For *t*-tests and ANOVAs, the data distribution was assumed to be normal, but this was not formally tested. We used several variants of permutation tests: in Fig. 7b,e,f, we permuted condition labels (REST and MOVIE); in Fig. 7g, we permuted system labels; in Supplementary Figs. 21 and 22, we mapped edge communities into a region-by-region matrix and permuted its rows and columns before extracting the permuted edge community labels (Supplementary Figs. 18 and 24). For permutation tests, observed values were *z* scored with respect to the mean and s.d. estimated for the null distribution and converted into *P* values.

Reporting Summary. Further information on research design is available in the Nature Research Reporting Summary linked to this article.

Data availability

All imaging data come from publicly available, open access repositories. Human Connectome Project data can be accessed at <https://db.humanconnectome.org/app/template/Login.vm> after signing a data use agreement. Midnight Scan Club data can be accessed via OpenNeuro at <https://openneuro.org/datasets/ds000224> versions/1.0.1. The Healthy Brain Network Serial Scanning Initiative data can be accessed at https://fcon_1000.projects.nitrc.org/indi/hbn_ssi/download.html.

Code availability

Code to compute eFC and its related derivatives has been made available at <https://github.com/brain-networks>.

References

- Shine, J. M. et al. Human cognition involves the dynamic integration of neural activity and neuromodulatory systems. *Nat. Neurosci.* **22**, 289–296 (2019).
- Davison, E. N. et al. Brain network adaptability across task states. *PLoS Comput. Biol.* **11**, e1004029 (2015).
- Glasser, M. F. et al. The minimal preprocessing pipelines for the Human Connectome Project. *Neuroimage* **80**, 105–124 (2013).
- Robinson, E. C. et al. MSM: a new flexible framework for multimodal surface matching. *Neuroimage* **100**, 414–426 (2014).
- Esteban, O. et al. fMRIprep: a robust preprocessing pipeline for functional MRI. *Nat. Methods* **16**, 111–116 (2019).
- Gorgolewski, K. et al. Nipype: a flexible, lightweight and extensible neuroimaging data processing framework in Python. *Front. Neuroinform.* **5**, 13 (2011).
- Abraham, A. et al. Machine learning for neuroimaging with scikit-learn. *Front. Neuroinform.* **8**, 14 (2014).
- Avants, B. B., Epstein, C. L., Grossman, M. & Gee, J. C. Symmetric diffeomorphic image registration with cross-correlation: evaluating automated labeling of elderly and neurodegenerative brain. *Med. Image Anal.* **12**, 26–41 (2008).
- Tustison, N. J. et al. N4ITK: improved N3 bias correction. *IEEE Trans. Med. Imaging* **29**, 1310–1320 (2010).
- Dale, A. M., Fischl, B. & Sereno, M. I. Cortical surface-based analysis: I. Segmentation and surface reconstruction. *Neuroimage* **9**, 179–194 (1999).
- Klein, A. et al. Mindboggling morphometry of human brains. *PLoS Comput. Biol.* **13**, e1005350 (2017).
- Fonov, V. S., Evans, A. C., McKinstry, R. C., Almlí, C. & Collins, D. Unbiased nonlinear average age-appropriate brain templates from birth to adulthood. *Neuroimage* **47**, S102 (2009).
- Zhang, Y., Brady, M. & Smith, S. Segmentation of brain MR images through a hidden Markov random field model and the expectation–maximization algorithm. *IEEE Trans. Med. Imaging* **20**, 45–57 (2001).
- Jenkinson, M., Bannister, P., Brady, M. & Smith, S. Improved optimization for the robust and accurate linear registration and motion correction of brain images. *Neuroimage* **17**, 825–841 (2002).
- Wang, S. et al. Evaluation of field map and nonlinear registration methods for correction of susceptibility artifacts in diffusion MRI. *Front. Neuroinform.* **11**, 17 (2017).
- Treiber, J. M. et al. Characterization and correction of geometric distortions in 814 diffusion weighted images. *PLoS ONE* **11**, e0152472 (2016).
- Greve, D. N. & Fischl, B. Accurate and robust brain image alignment using boundary-based registration. *Neuroimage* **48**, 63–72 (2009).
- Power, J. D. et al. Methods to detect, characterize, and remove motion artifact in resting state fMRI. *Neuroimage* **84**, 320–341 (2014).
- Esteban, O. et al. MRIQC: advancing the automatic prediction of image quality in MRI from unseen sites. *PLoS ONE* **12**, e0184661 (2017).
- Parkes, L., Fulcher, B., Yücel, M. & Fornito, A. An evaluation of the efficacy, reliability, and sensitivity of motion correction strategies for resting-state functional MRI. *Neuroimage* **171**, 415–436 (2018).
- Yeo, B. T. et al. The organization of the human cerebral cortex estimated by intrinsic functional connectivity. *J. Neurophysiol.* **106**, 1126–1165 (2011).
- Fischl, B. et al. Automatically parcellating the human cerebral cortex. *Cereb. Cortex* **14**, 11–22 (2004).
- Lindquist, M. A., Geuter, S., Wager, T. D. & Caffo, B. S. Modular preprocessing pipelines can reintroduce artifacts into fMRI data. *Hum. Brain Mapp.* **40**, 2358–2376 (2019).
- Satterthwaite, T. D. et al. An improved framework for confound regression and filtering for control of motion artifact in the preprocessing of resting-state functional connectivity data. *Neuroimage* **64**, 240–256 (2013).
- Gopalan, P. K. & Blei, D. M. Efficient discovery of overlapping communities in massive networks. *Proc. Natl. Acad. Sci. USA* **110**, 14534–14539 (2013).
- Yang, J. & Leskovec, J. Overlapping communities explain core-periphery organization of networks. *Proc. IEEE* **102**, 1892–1902 (2014).
- Psorakis, I., Roberts, S., Ebden, M. & Sheldon, B. Overlapping community detection using Bayesian non-negative matrix factorization. *Phys. Rev. E* **83**, 066114 (2011).
- Najafi, M., McMenamin, B. W., Simon, J. Z. & Pessoa, L. Overlapping communities reveal rich structure in large-scale brain networks during rest and task conditions. *Neuroimage* **135**, 92–106 (2016).
- Guimera, R. & Amaral, L. A. N. Functional cartography of complex metabolic networks. *Nature* **433**, 895–900 (2005).
- Shinn, M. et al. Versatility of nodal affiliation to communities. *Sci. Rep.* **7**, 1–10 (2017).
- Pedersen, M., Zalesky, A., Omidvarnia, A. & Jackson, G. D. Multilayer network switching rate predicts brain performance. *Proc. Natl. Acad. Sci. USA* **115**, 13376–13381 (2018).
- Reichardt, J. & Bornholdt, S. Statistical mechanics of community detection. *Phys. Rev. E* **74**, 016110 (2006).
- Traag, V. A., Van Dooren, P. & Nesterov, Y. Narrow scope for resolution-limit-free community detection. *Phys. Rev. E* **84**, 016114 (2011).
- Bazzi, M. et al. Community detection in temporal multilayer networks, with an application to correlation networks. *Multiscale Model. Simul.* **14**, 1–41 (2016).
- Betzel, R. F. et al. The community structure of functional brain networks exhibits scale-specific patterns of inter-and intra-subject variability. *Neuroimage* **202**, 115990 (2019).
- Mucha, P. J., Richardson, T., Macon, K., Porter, M. A. & Onnela, J.-P. Community structure in time-dependent, multiscale, and multiplex networks. *Science* **328**, 876–878 (2010).
- Smith, S. M. et al. A positive–negative mode of population covariation links brain connectivity, demographics and behavior. *Nat. Neurosci.* **18**, 1565–1567 (2015).

Acknowledgements

This research was supported by the Indiana University Office of the Vice President for Research Emerging Area of Research Initiative, Learning: Brains, Machines and Children (F.Z.E. and R.F.B.). This material is based on work supported by the National Science Foundation Graduate Research Fellowship under grant no. 1342962 (J.F.). This research was supported, in part, by the Lilly Endowment, through its support for the Indiana University Pervasive Technology Institute and, in part, by the Indiana METACyt Initiative. The Indiana METACyt Initiative at Indiana University was also supported, in part, by the Lilly Endowment. Data were provided, in part, by the Human Connectome Project, WU-Minn Consortium (principal investigators: D. Van Essen and K. Ugurbil; 1U54MH091657), funded by the 16 National Institutes of Health (NIH) institutes and centers that support the NIH Blueprint for Neuroscience Research and by the McDonnell

Center for Systems Neuroscience at Washington University. We thank B. Mišić for reading an early version of this manuscript.

Author contributions

J.F. and R.F.B. conceived of the study, processed data, carried out all analyses and wrote the first draft of the manuscript. F.Z.E., Y.J. and O.S. contributed to project direction via discussion. All authors helped revise and write the submitted manuscript.

Competing interests

The authors declare no competing interests.

Additional information

Supplementary information is available for this paper at <https://doi.org/10.1038/s41593-020-00719-y>.

Correspondence and requests for materials should be addressed to R.F.B.

Peer review information *Nature Neuroscience* thanks Lucina Uddin, Andrew Zalesky, and the other, anonymous, reviewer(s) for their contribution to the peer review of this work.

Reprints and permissions information is available at www.nature.com/reprints.

Reporting Summary

Nature Research wishes to improve the reproducibility of the work that we publish. This form provides structure for consistency and transparency in reporting. For further information on Nature Research policies, see [Authors & Referees](#) and the [Editorial Policy Checklist](#).

Statistics

For all statistical analyses, confirm that the following items are present in the figure legend, table legend, main text, or Methods section.

n/a Confirmed

- The exact sample size (n) for each experimental group/condition, given as a discrete number and unit of measurement
- A statement on whether measurements were taken from distinct samples or whether the same sample was measured repeatedly
- The statistical test(s) used AND whether they are one- or two-sided
Only common tests should be described solely by name; describe more complex techniques in the Methods section.
- A description of all covariates tested
- A description of any assumptions or corrections, such as tests of normality and adjustment for multiple comparisons
- A full description of the statistical parameters including central tendency (e.g. means) or other basic estimates (e.g. regression coefficient) AND variation (e.g. standard deviation) or associated estimates of uncertainty (e.g. confidence intervals)
- For null hypothesis testing, the test statistic (e.g. F , t , r) with confidence intervals, effect sizes, degrees of freedom and P value noted
Give P values as exact values whenever suitable.
- For Bayesian analysis, information on the choice of priors and Markov chain Monte Carlo settings
- For hierarchical and complex designs, identification of the appropriate level for tests and full reporting of outcomes
- Estimates of effect sizes (e.g. Cohen's d , Pearson's r), indicating how they were calculated

Our web collection on [statistics for biologists](#) contains articles on many of the points above.

Software and code

Policy information about [availability of computer code](#)

Data collection

All data used in this study is publicly available. The authors of this study did not write custom code to collect any of this data; therefore the authors did not use software for data collection.

Data analysis

Human Connectome Project data are provided already minimally preprocessed at the ConnectomeDB (<https://db.humanconnectome.org/app/template/Login.vm>). Midnight Scan Club and Healthy Brain Network fMRI data were preprocessed with fMRIprep version 1.3.2. fMRIprep can be found here: <https://github.com/poldracklab/fmriprep>. fMRIprep uses Nipype 1.1.9, Nilearn 0.5.0, ANTs 2.2.0, FreeSurfer 6.0.1, FSL 5.0.9, AFNI v16.2.07, and Mindboggle [RRID:SCR_002438]. Subject specific parcellations were fit with FreeSurfer 6.0.1 using code available here: <https://github.com/faskowitz/multiAtlasTT> and data available here: https://figshare.com/articles/multiAtlasTT_data_hcptrained/7552853. fMRI data were nuisance regressed with code available here: <https://github.com/faskowitz/app-fmri-2-mat> which uses Nilearn's signal.clean, from Nilearn 0.5.0. Custom MATLAB (version 2019a) code was used for analyzing eFC. Upon manuscript acceptance, functions to generate and analyze edge time series and eFC will be released as a repository on the Brain Networks & Behavior Lab Github: <https://github.com/brain-networks/>. Custom MATLAB to fit alternative overlapping algorithms is available here: https://github.com/faskowitz/overlap_on_NxN_func.

For manuscripts utilizing custom algorithms or software that are central to the research but not yet described in published literature, software must be made available to editors/reviewers. We strongly encourage code deposition in a community repository (e.g. GitHub). See the Nature Research [guidelines for submitting code & software](#) for further information.

Data

Policy information about [availability of data](#)

All manuscripts must include a [data availability statement](#). This statement should provide the following information, where applicable:

- Accession codes, unique identifiers, or web links for publicly available datasets
- A list of figures that have associated raw data
- A description of any restrictions on data availability

All imaging data come from publicly-available, open-access repositories. Human Connectome Project data can be accessed via (<https://db.humanconnectome.org/>

Field-specific reporting

Please select the one below that is the best fit for your research. If you are not sure, read the appropriate sections before making your selection.

Life sciences Behavioural & social sciences Ecological, evolutionary & environmental sciences

For a reference copy of the document with all sections, see nature.com/documents/nr-reporting-summary-flat.pdf

Life sciences study design

All studies must disclose on these points even when the disclosure is negative.

Sample size

Three human neuroimaging datasets were used in this study: Human Connectome Project (HCP), Midnight Scan Club (MSC), and Health Brain Network Serial Scanning Initiative (HBN). For HCP, we used a publicly available list of 100 unrelated subjects. For MSC, the dataset consists of 10 subjects. For HBN, the dataset consists of 13 subjects; due to limited availability of low motion fMRI scans, 3 subjects of HBN were excluded. Each of the three datasets were chosen to provide data to demonstrate aspects of the novel eFC construct. The 100 unrelated HCP subjects were utilized for constructing eFC from a large unrelated (the data is a subset of a large twins study) cohort of high-quality neuroimaging data. The MSC data was utilized for demonstrating reliability of eFC, given that MSC subjects have 10 resting state scans each. The HBN dataset was utilized from demonstrating how passive movie watching could affect eFC, since for this dataset multiple resting and movie-watching scans were acquired. No statistical methods were used to pre-determine sample sizes, but our sample sizes are similar to those reported in previous publications and represent either all usable data (MSC, HBN) or a subset preselected by the study coordinators (HCP)

Data exclusions

Three subjects of the HBN dataset were excluded from our study for having little to no MRI data that passed our data exclusion criteria. Individual HBN fMRI were excluded based on image quality metrics (IQMs) output from MRIQC. The MRIQC package was designed to automatically provide IQMs and individual and group visual reports using reproducible containerization technology. The following IQMs were used: dvars, tsnr, fd mean, aor, aqi,, snr, and etc. Individual scans were excluded if the IQMs for the scan exceeded 1.5 times the inter-quartile range of the distribution (in the adverse direction) of a particular IQM across the dataset, for five or more of the IQMs. Individual scans were also excluded if more than 25% of frames exceeded 0.2mm frame-wise displacement. Code to implement this filtering can be found at: https://github.com/faskowitz/filter_mriqc_res. The IQM exclusion criteria have not been employed in this manner in a previous study. The framewise displacement exclusion criteria were partly based on Parkes et al. (2018) NeuroImage. These exclusion criteria were pre-established for HBN. All scans from HCP and MSC were retained; this was also pre-established. All data were visually inspected for artifacts. Furthermore, in Supplementary Figure 2 we demonstrate that after censoring high motion frames in the HCP data, the correlation of edge amplitude with motion does not substantially change.

Replication

Supplemental Figure 3 shows the correlation of eFC data across three independent datasets (HCP, MSC, and HBN). Supplemental Figure 4 shows the correlation of eFC data from HCP, processed with different nuisance regression strategies. Supplemental Figure 11 shows the normalized entropy maps for each dataset (HCP, MSC, HBN). Supplemental Figure 13 shows the normalized entropy maps across number of communities (k) in the HCP dataset. Supplemental Figure 14 shows the normalized entropy maps across three alternative parcellations (Desikan-Killiany, Destrieux, and Brainnetome) of the cortex. The authors consider all of these to be instances of successful replication regarding concepts related to the novel eFC construct.

Randomization

Subjects were not partitioned into groups. Data from each cohort (HCP, MSC, HBN) were analyzed separately. This choice was made so as to not mix data across MRI machine and MRI acquisition parameters.

Blinding

Data analysis was not performed blind to the conditions of the experiments. Blinding was not relevant because subjects were not evaluated based on group membership and blinding was not applicable to the whole-group analyses reported in this study.

Reporting for specific materials, systems and methods

We require information from authors about some types of materials, experimental systems and methods used in many studies. Here, indicate whether each material, system or method listed is relevant to your study. If you are not sure if a list item applies to your research, read the appropriate section before selecting a response.

Materials & experimental systems

- | | |
|-------------------------------------|---|
| n/a | Involved in the study |
| <input checked="" type="checkbox"/> | <input type="checkbox"/> Antibodies |
| <input checked="" type="checkbox"/> | <input type="checkbox"/> Eukaryotic cell lines |
| <input checked="" type="checkbox"/> | <input type="checkbox"/> Palaeontology |
| <input checked="" type="checkbox"/> | <input type="checkbox"/> Animals and other organisms |
| <input type="checkbox"/> | <input checked="" type="checkbox"/> Human research participants |
| <input checked="" type="checkbox"/> | <input type="checkbox"/> Clinical data |

Methods

- | | |
|-------------------------------------|--|
| n/a | Involved in the study |
| <input checked="" type="checkbox"/> | <input type="checkbox"/> ChIP-seq |
| <input checked="" type="checkbox"/> | <input type="checkbox"/> Flow cytometry |
| <input type="checkbox"/> | <input checked="" type="checkbox"/> MRI-based neuroimaging |

Human research participants

Policy information about [studies involving human research participants](#)

Population characteristics

The Human Connectome Project (HCP) aimed to collect healthy adult twins, ages 22-25 years old (Van Essen, 2012). The definition of "healthy" was broad, in order to collect a sample representative of the United States population in terms of behavior, ethnic, and socioeconomic diversity. In this study, a provided subset of subjects called the "Unrelated 100" was used. This subset has the following characteristics: 54% female; mean age = 29.11 ± 3.67 ; age range = 22-36. The Midnight Scan Club (MSC) consists of 10 participants who were healthy, right-handed, and aged 24-34 years old. Demographic information can be found in Gordon 2017, Table 1. The Healthy Brain Network Serial Scanning initiative (HBN) consists of 13 participants, aged 18-45 years old, who were used as pilot subjects for the wider Healthy Brain Network dataset collection (O'Connor 2017). Subject demographics can be found at: <http://gigadb.org/dataset/100259>

Recruitment

HCP subjects were recruited from the Missouri Department of Health and Senior Services Bureau of Vital Records. MSC subjects were recruited from the Washington University in St. Louis community. HBN subjects were recruited from the community participating in the wider Healthy Brain Network project. These details can be found at: http://fcon_1000.projects.nitrc.org/indi/cmi_healthy_brain_network/Recruitment.html The authors of the present study did not collect any of the primary imaging data nor did they conduct recruitment of subjects. Therefore, the authors are not knowledgeable about possible self-selection biases or other biases associated with the data collection of these three cohorts. Based on the previously described replications conducted on three independently acquired cohorts (across scanner strength as well), we would estimate that potential biases related to recruitment would not likely impact the main results of the study.

Ethics oversight

HCP was approved by the Washington University Institutional Review Board. MSC was approved by Washington University School of Medicine Human Studies Committee and Institutional Review Board. HBN was approved by Chesapeake Institutional Review Board.

Note that full information on the approval of the study protocol must also be provided in the manuscript.

Magnetic resonance imaging

Experimental design

Design type

In this study, we used resting state scans (fixation cross, eyes open) and a movie watching task ("Raiders of the Lost Ark").

Design specifications

No blocks were used in this study

Behavioral performance measures

Behavioral measures were used were not used for the main findings of this study. In Supplementary Figures 21-23, we present an exploratory analysis on the relationship between eFC and principle components of behavioral scores in HCP subjects. Principal components analysis was performed on the following behavioral performance measures (n=209), which are available as HCP unrestricted measures: MMSE_Score, PSQI_Score, PSQI_Comp1, PSQI_Comp2, PSQI_Comp3, PSQI_Comp4, PSQI_Comp5, PSQI_Comp6, PSQI_Comp7, PSQI_Min2Asleep, PSQI_AmtSleep, PSQI_Latency30Min, PSQI_WakeUp, PSQI_Bathroom, PSQI_Breathe, PSQI_Snore, PSQI_TooCold, PSQI_TooHot, PSQI_BadDream, PSQI_Pain, PSQI_Other, PSQI_Quality, PSQI_SleepMeds, PSQI_DayStayAwake, PSQI_DayEnthusiasm, PSQI_BedPtnrRmate, PicSeq_Unadj, PicSeq_AgeAdj, CardSort_Unadj, CardSort_AgeAdj, Flanker_Unadj, Flanker_AgeAdj, PMAT24_A_CR, PMAT24_A_SI, PMAT24_A_RTCR, ReadEng_Unadj, ReadEng_AgeAdj, PicVocab_Unadj, PicVocab_AgeAdj, ProcSpeed_Unadj, ProcSpeed_AgeAdj, DDisc_SV_1mo_200, DDisc_SV_6mo_200, DDisc_SV_1yr_200, DDisc_SV_3yr_200, DDisc_SV_5yr_200, DDisc_SV_10yr_200, DDisc_SV_1mo_40K, DDisc_SV_6mo_40K, DDisc_SV_1yr_40K, DDisc_SV_3yr_40K, DDisc_SV_5yr_40K, DDisc_SV_10yr_40K, DDisc_AUC_200, DDisc_AUC_40K, VSPLIT_TC, VSPLIT_CRTE, VSPLIT_OFF, SCPT_TP, SCPT_TN, SCPT_FP, SCPT_FN, SCPT_TPRT, SCPT_SEN, SCPT_SPEC, SCPT_LRNR, IWRD_TOT, IWRD_RTC, ListSort_Unadj, ListSort_AgeAdj, CogFluidComp_Unadj, CogFluidComp_AgeAdj, CogEarlyComp_Unadj, CogEarlyComp_AgeAdj, CogTotalComp_Unadj, CogTotalComp_AgeAdj, CogCrystalComp_Unadj, CogCrystalComp_AgeAdj, ER40_CR, ER40_CRT, ER40ANG, ER40FEAR, ER40HAP, ER40NOE, ER40SAD, AngAffect_Unadj, AngHostil_Unadj, AngAggr_Unadj, FearAffect_Unadj, FearSomat_Unadj, Sadness_Unadj, LifeSatisf_Unadj, MeanPurp_Unadj, PosAffect_Unadj, Friendship_Unadj, Loneliness_Unadj, PerchHostil_Unadj, PercReject_Unadj, EmotSupp_Unadj, InstruSupp_Unadj, PercStress_Unadj, SelfEff_Unadj, Emotion_Task_Acc, Emotion_Task_Median_RT, Emotion_Task_Face_Acc, Emotion_Task_Face_Median_RT, Emotion_Task_Shape_Acc, Emotion_Task_Shape_Median_RT, Gambling_Task_Perc_Larger, Gambling_Task_Perc_Smaller, Gambling_Task_Median_RT_Larger, Gambling_Task_Reward_Perc_Larger, Gambling_Task_Reward_Median_RT_Larger, Gambling_Task_Reward_Perc_Smaller, Gambling_Task_Punish_Perc_Larger, Gambling_Task_Punish_Median_RT_Larger, Gambling_Task_Punish_Perc_Smaller, Language_Task_Acc, Language_Task_Median_RT, Language_Task_Story_Acc, Language_Task_Story_Median_RT, Language_Task_Story_Avg_Difficulty_Level, Language_Task_Math_Acc, Language_Task_Math_Median_RT, Language_Task_Math_Avg_Difficulty_Level, Relational_Task_Acc, Relational_Task_Median_RT, Relational_Task_Match_Acc, Relational_Task_Match_Median_RT, Relational_Task_Rel_Acc, Relational_Task_Rel_Median_RT, Social_Task_Perc_Random, Social_Task_Perc_TOM, Social_Task_Perc_Unsure, Social_Task_Median_RT_TOM, Social_Task_Random_Perc_Random, Social_Task_Random_Perc_TOM, Social_Task_Random_Perc_Unsure, Social_Task_TOM_Perc_Random, Social_Task_TOM_Perc_TOM, Social_Task_TOM_Median_RT_TOM, Social_Task_TOM_Perc_Unsure, WM_Task_Acc, WM_Task_Median_RT, WM_Task_2bk_Acc, WM_Task_2bk_Median_RT, WM_Task_0bk_Acc, WM_Task_0bk_Median_RT,

WM_Task_Obk_Body_Acc, WM_Task_Obk_Body_Acc_Target, WM_Task_Obk_Body_Acc_Nontarget, WM_Task_Obk_Face_Acc, WM_Task_Obk_Face_Acc_Target, WM_Task_Obk_Face_ACC_Nontarget, WM_Task_Obk_Place_Acc, WM_Task_Obk_Place_Acc_Target, WM_Task_Obk_Place_Acc_Nontarget, WM_Task_Obk_Tool_Acc, WM_Task_Obk_Tool_Acc_Target, WM_Task_Obk_Tool_Acc_Nontarget, WM_Task_2bk_Body_Acc, WM_Task_2bk_Body_Acc_Target, WM_Task_2bk_Body_Acc_Nontarget, WM_Task_2bk_Face_Acc, WM_Task_2bk_Face_Acc_Target, WM_Task_2bk_Face_Acc_Nontarget, WM_Task_2bk_Place_Acc, WM_Task_2bk_Place_Acc_Target, WM_Task_2bk_Place_Acc_Nontarget, WM_Task_2bk_Tool_Acc, WM_Task_2bk_Tool_Acc_Target, WM_Task_2bk_Tool_Acc_Nontarget, WM_Task_Obk_Body_Median_RT, WM_Task_Obk_Body_Median_RT_Nontarget, WM_Task_Obk_Face_Median_RT, WM_Task_Obk_Face_Median_RT_Nontarget, WM_Task_Obk_Place_Median_RT_Nontarget, WM_Task_Obk_Tool_Median_RT, WM_Task_Obk_Tool_Median_RT_Nontarget, WM_Task_2bk_Body_Median_RT, WM_Task_2bk_Face_Median_RT, WM_Task_2bk_Face_Median_RT_Nontarget, WM_Task_2bk_Place_Median_RT, WM_Task_2bk_Place_Median_RT_Nontarget, WM_Task_2bk_Tool_Median_RT, WM_Task_2bk_Tool_Median_RT_Nontarget, Endurance_Unadj, Endurance_AgeAdj, GaitSpeed_Comp, Dexterity_Unadj, Dexterity_AgeAdj, Strength_Unadj, Strength_AgeAdj, NEOFAC_A, NEOFAC_O, NEOFAC_C, NEOFAC_N, NEOFAC_E, Odor_Unadj, Odor_AgeAdj, PainIntens_RawScore, PainInterf_Tscore, Taste_Unadj, Taste_AgeAdj, Mars_Log_Score, Mars_Errs, Mars_Final

Acquisition

Imaging type(s)

structural, functional

Field strength

3T, 1.5T

Sequence & imaging parameters

HCP: Resting state fMRI (rsfMRI) data was acquired with a gradient-echo EPI sequence (run duration = 14:33 min, TR = 720 ms, TE = 33.1 ms, flip angle = 52 degrees, 2 mm isotropic voxel resolution, multiband factor = 8) with eyes open and instructions to fixate on a cross. Images were collected on a 3T Siemens Connectome Skyra with a 32-channel head coil. MSC: rsfMRI scans were collected with a gradient-echo EPI sequence (run duration = 30 min, TR = 2200 ms, TE = 27 ms, flip angle = 90 degrees, 4 mm isotropic voxel resolution) with eyes open and with eye tracking recording to monitor for prolonged eye closure (to assess drowsiness). Images were collected on a 3T Siemens Trio. HBN: rsfMRI and movie watching (mvfMRI) were acquired with a gradient-echo EPI sequence (run duration rsfMRI = 10:18 min, mvfMRI = 20 min per segment, TR = 1450 ms, TE = 40 ms, flip angle = 55, 2.46x2.46x2.5 mm voxel resolution, multi-band factor = 3) with subjects instructed to keep their eyes open and gazed directed towards a cross during the rsMRI scan. Images were collected on a 1.5T Siemens Avanto with a 32-channel head coil.

Area of acquisition

whole-brain

Diffusion MRI

Used

Not used

Preprocessing

Preprocessing software

Functional images in the HCP were processed with the HCP pipelines and downloaded after the 1200 subject data release. The HCP pipelines utilize FSL, Connectome Workbench, and custom MATLAB. Functional images in the MSC and HBN datasets were preprocessed using fMRIprep 1.3.2 [90], which is based on Nipype 1.1.9 [91]. Internal operations of fMRIprep use Nilearn 0.5.0, ANTs 2.2.0, FreeSurfer 6.0.1, FSL 5.0.9, and AFNI v16.2.07. For more details about the pipeline, see the section corresponding to workows in fMRIprep's documentation, for version 1.3.2.

Normalization

Within the fMRIprep workflow, ANTs is used to align functional images to the MNI Asymmetrical template version 2009c. For HCP, FSL FNIRT is used to align functional images in the FSL MNI template and furthermore, multi-modal registration is used to align surface functional data to the fs_LR surface space.

Normalization template

For HCP, fMRI data was analyzed after linear alignment (AC-PC) to the FSL MNI template. For MSC and HBN, fMRI data was analyzed in each subject's T1w space.

Noise and artifact removal

We employed a 36-parameter nuisance regression strategy described Satterthwaite 2013 and shown to be an effective strategy in Parkes 2018. In Supplemental Figure 4, we present a scatter plot comparing eFC values derived from data processed with this 36-parameter strategy to eFC values derived from data processed with an ICA-FIX de-noising strategy.

Volume censoring

We used spike regression in place of volume censoring. A spike regressor was added for each fMRI frame exceeding a motion threshold (HCP = 0.25 mm root mean squared displacement, MSC, HBN = 0.5 mm framewise displacement)

Statistical modeling & inference

Model type and settings

We employ k-means cluster on the rescaled eigenvectors of the eFC matrix data. The k-means model assumes that clusters can be formed around k number of centroids in the data. This clustering was repeated 250 times and the centroid partition (most similar to all other partitions) was retained. Since the number of clusters is a free parameter, we show results with 2, 4, 6, 8, 10, and 12 clusters in the manuscript.

Effect(s) tested

In Figure 7 and Supplementary Figure 18, we demonstrate the difference between eFC calculated from a change in task

Effect(s) tested

conditions (resting state versus movie watching) for HBN subjects.

Specify type of analysis: Whole brain ROI-based BothStatistic type for inference
(See [Eklund et al. 2016](#))

Voxel-wise or cluster-wise inference was not performed in this study.

Correction

In the comparison of rest versus movie eFC, we report nodes where eFC values significantly change based on a FDR (Benjamini-Hochberg) threshold alpha=0.05 (Supplemental Figure 18). Furthermore, we employed a constrained null model to randomize edge values while presenting certain edge relationships (see Supplemental Figure 18).

Models & analysis

n/a | Involved in the study

- Functional and/or effective connectivity
- Graph analysis
- Multivariate modeling or predictive analysis

Functional and/or effective connectivity

In this study, we propose a measure called eFC, which is conceptually related to Pearson correlation. The relation to Pearson correlation is explained in the manuscript. In Figure 1c, we compare eFC values to a multiplication of the edges' corresponding nFC values (Pearson correlation). We note that a direct comparison of eFC to nFC values is not possible, due to different data dimensionality.

Graph analysis

We construct an edge-by-edge graph (eFC matrix), which is weighted and undirected with entries from -1 to 1. These values represent the magnitude of co-fluctuation between edge time series. In this manuscript, we describe a method to apply community detection to this matrix. In Supplemental Figure 20, we provide examples of other network measures that can be applied to the eFC matrix and mapped back to the NxN space.